NSG-1483

P-66

GRADUATE AERONAUTICAL LABORATORIES

CALIFORNIA INSTITUTE OF TECHNOLOGY

(NASA-CR-179911) OBSERVATION OF THE INITIATION AND PROGRESSION OF DAMAGE IN COMPRESSIVELY LOADED COMPOSITE PLATES CONTAINING A CUTOUT Progress Report (California Inst. of Tech.) 66 p CSCL 20K

N87-12022

Unclas

G3/39 44927

Firestone Flight Sciences Laboratory

Guggenheim Aeronautical Laboratory

Karman Laboratory of Fluid Mechanics and Jet Propulsion

Pasadena

SM Report 86-34

OBSERVATION OF THE INITIATION AND PROGRESSION OF DAMAGE IN COMPRESSIVELY LOADED COMPOSITE PLATES CONTAINING A CUTOUT

Anthony Waas *

Charles Babcock. jr **

Progress report

Grant: NSG 1483

November 1986

Graduate Aeronautical Laboratories

California Institute of Technology

Pasadena, California 91125

* *Graduate Research Assistant*

** *Professor of Aeronautics and Applied Mechanics*

Abstract

A series of experiments were carried out to determine the mechanism of failure in compressively loaded laminated plates with a circular cutout. Real time holographic interferometry and photomicrography are used to observe the progression of failure. These observations together with post experiment plate sectioning and deplying for interior damage observation provide useful information for modelling the failure process.

It is revealed that the failure is initiated as a localised instability in the zero layers, at the hole surface. With increasing load extensive delamination cracking is observed. The progression of failure is by growth of these delaminations induced by delamination buckling. Upon reaching a critical state, catastrophic failure of the plate is observed. The levels of applied load and the rate at which these events occur depend on the plate stacking sequence.

1.1 Introduction

The use of Graphite/Epoxy laminates in various fields of engineering has posed a new challenge to engineering design. In many instances, it is necessary to look for new techniques to characterise these materials which differ from isotropic , homogeneous materials in their response to mechanical load. Extensive research programs are being carried out throughout the country aimed at improving the understanding of the mechanics of Composite Materials.

One situation where these laminates exhibit a different type of behaviour is when they are subjected to compressive loads. One or several competing modes of failure are present and the researcher is left with the task of identifying the most important aspect of the failure process from a design standpoint. When structural components are made out of these laminates it is seldom that they will persist in an environment free of stress concentrations. Stress raisers can be lethal and are potential sites where damage can initiate in a structure.

The open hole strengths of these laminates has been the subject of numerous investigations [1-4]. Figure 1 depicts ultimate load carrying capacity of these laminates as a function of the normalised hole diameter. *Mikulas* [5], has shown that the results could be bounded by simple criteria based on notch sensitivity. If the material is notch insensitive, the failure strains are directly proportional to the reduction in cross-sectional area, while if the material is notch sensitive then it is postulated that the material fails when the strain concentration at the hole edge equals the failure strain of the material. It is seen that the latter assumption is non-conservative in that the failure strain is underestimated for (a/w) ratios less than 0.4 . This situation indicates the possibility that the strain concentration effect alone cannot possibly account for the failure process and that a localised failure mechanism may be present. Based on this premise Starnes et al [1] carried out open hole strength testing of these laminates and reported a *shear crippling* type of failure to be prevalent in the vicinity of the hole prior to catastrophic failure. This conclusion was based on post-mortem examination of damaged specimen.

In these and other similar investigations no attempt has been made to follow the progression of failure. The progressive nature of failure, in many cases, by various stages is a characteristic property of laminated composites. Several different failure processes are prevalent when these laminates are stressed and what is required is to identify the key aspects of failure in a particular situation.

Motivated from such an understanding, the present work is a detailed experimental investigation to understand the initiation and propagation of failure in laminates in the presence of a stress raiser. The stress concentration effect is produced by choosing a flat plate with a centered circular hole and subjecting it to an inplane compressive load. The hole is carefully cut in order to insure that excessive local damage does not occur during the machining process. The damage initiation and propagation throughout the entire load history is studied via real time *Holographic Interferometry* and *Photomicrography* of the hole surface. The results thus obtained are substantiated by post experiment examination of the damaged specimen *Ultrasonically* and under an *Optical Microscope.*

In the sections to follow, the Experiments and associated methodology is presented first. Pertinent details are given where necessary but no attempt is made to go into extensive details. Thus, the reader is refered to relevant texts on Holography, Ultrasonic scanning etc. for a detailed treatment of the subject. We emphasise here that our main goal is to capture the phenomenological aspects of the failure process as opposed to conducting a parameter study.

1.2 The Experiment

1.2.1 Assembly

Figure 2 is a photograph showing the arrangement of the various devices used in the experiment. On a pneumatically vibration isolated table, optical components are arranged to make a hologram and generate interferograms of the test specimen which is loaded by a table top compression device. An optical microscope is mounted on a tripod which is situated adjacent to the optical table by the testing machine. A 35 *mm* motor driven SLR camera attached to the microscope is used to take photographs of the test specimen hole surface, during the testing sequence. Recording and developing of the hologram is done on a thermoplastic plate which is housed in the body of the instant recording device(IRD) as marked in Figure 2. This device which is electronically controlled replaces the conventional wet chemical processes which are used had the recording being done on a photographic plate. A video camera placed behind the thermoplastic plate views the test specimen through the hologram. A VCR records the interferometric pattern generated during the loading sequence. A TV monitor is used to view the interferograms during a typical test, which enables testing to be done interactively. In the following sections the main components of the experiment are described.

1.2.2 Specimen

The multi-layered laminated plates used in the tests were supplied by NASA-Langley Research Center. The composition of the laminae in the specimen consisted of Thornel-300 graphite fibers preimpregnated with American Cyanamide BP 907 epoxy resin. This laminate is typical of those used in the Aerospace Industry. Two types of lamina stacking sequence were used in the tests. The first designated Type A is 48 ply $[+45/-45/0/0/+45/-45/0/0/+45/-45/0/90]_{2s}$ while the other , Type B is obtained by rotating the first sequence by ninety degrees, the angles being measured with respect to the loading direction counterclockwise. Diamond impregnated core drills and saws are used for machining the specimen. Two sizes of specimen are used. The first designated "S" is 7.62 $cm \times 10.2$ cm and the other "L" is 12.7 cm $\times$ 15.3 cm.

1.2.3 Specimen Supports

The laminated plates need to be supported in a manner that allows a smooth load transfer from the testing machine on to the plates. To do this specimen holders made of mild steel are used in these tests. The diameters of the holders are chosen to be the widths of the specimen. The holders contain grooves of 1.27 cm depth and widths large enough to accomodate the specimen and the thin layers of bonding agent. The test specimen are inserted into the grooves and bonded to the support holders with DEVCON bonding agent. Edge stiffeners are attached to the sides of the specimen to avoid plate buckling. These stiffeners increase the flexural stiffness of the plate but carry no load. A typical set of edge stiffeners is shown in Figure 3.

1.2.3 Testing Machine

The use of real time holographic interferometry requires vibration isolation of test specimen and testing device. As such, a special purpose testing device was designed and constructed for this purpose. Both tension and compression load can be applied using this device. At the commencement of a test one end of the specimen support holders is inserted into an adapter which threads onto the actuator arm of the loading device. A ball joint is attached to the other end. The mating part of the ball joint is positioned at the center of a 100,000 lbf (445 kN) load cell. The load cell is mounted on one of the flanged box beams of the testing machine. A photograph of the testing machine and accessories positioned on the optical table is shown in Figure 4a. A photograph of a specimen mounted as described earlier with the balljoint arrangement is shown in Figure 5.

The load-time history is regulated through a servo controlled loading mechanism. The servo valve and associated accessories are mounted on a plate which fits on the cylinder of the loading device. A function generator is used to program the loading path. A picture of the servo valve and accessories is shown in Figure 4b.

1.2.4 Holographic Interferometry

Real time holographic interferometry is used in this study to record the out of plane displacement changes Δw of the specimen during the loading sequence. The revelant details of the technique as applicable to the present experiment is given in section **1.2** . One novelty in the present experiment is the use of an electronically controlled process in the recording and development of a hologram. In conventional holography a wet chemical process is used in the development of the photographic glass plates. The time consumed during this process which is of the order of 7-9 minutes, is a significant portion of the total duration of a test which is of the order 2 hours. During a continuous loading sequence, the information on the displacement history is lost during this development time. The electronic process refered to above and explained in the next section overcomes this drawback.

1.2.5 The Instant Recording Device

In the reconstruction process of a hologram the conventional Silver Halide photographic plates cause diffraction via an *amplitude grating* which is representative of the spatial distribution of light(amplitude and phase) that is emitted from the diffusely reflective surface of the object. However, the same task could be accomplished with a *Phase grating* i.e. , a surface contour variation which is representative of the light off of the object. This is the basic idea behind the success of the thermoplastic recording device. The device has several stages of operation as shown in Figure 6. Steps (a) through (d) require less than one minute - a considerable saving of time. Furthermore, with real time holographic interferometry, a complete deformation history of the object up to failure can be recorded. This is important in the study of composites which exhibit several stages of failure. There are four basic steps in the creation of a hologram with this device.

Step 1.

A uniform charge is deposited on the thermoplastic plate as shown in Figure 6a. A movable coronatron deposits this charge. A corresponding negative charge forms on the transparent electrical conductor which is connected to ground.

Step 2.

The plate is exposed. Charge passes through the photoconductor only in the illuminated areas (Figure 6b.).

Step 3.

Another charge is provided to the plate. Because the plate is now not exposed to the light the charge does not move across the photoconductor. Thus, the areas of the thermoplastic that were illuminated experience a greater electric field; the charge density is greater in the illuminated areas.

Step 4.

The development of the hologram is carried out by heating the thermoplastic plate. In areas where the electric field is greater, the heat softened thermoplastic becomes thinner(Figure 6d). This creates the surface contour variation which causes the diffraction of light in the reconstruction stage.

The *coronatron* is a device that consists of a wire anode running down the center of a slotted cylinder. The slot is oriented to face the thermoplastic plate. The slotted cylinder and plate are grounded and the anode is raised to a potential of several kilovolts. The resulting electric fields ionize the surrounding air, producing electrons and positive ions. The electrons are collected on the wire which results in a positive charge on the slotted cylinder and the thermoplastic plate (Figure 7).

The detailed structure of the thermoplastic plate is shown in Figure 8. On a quartz substrate, an optically transparent electrode of Indium-Tin oxide is deposited on top of which a 1 μm thick layer of trinitro-fluorenone doped photoconductive organic polymer is placed and finally a 0.7 μm thermoplastic layer is added. Metal electrodes are attached to each side of the transparent electrode which provides a ground plane for the coronatron. A current passed through the transparent electrode produces resistive heating sufficient to soften the thermoplastic.

The cycle of events explained above is sequenced by a control unit supplied with the recording device. Dry Nitrogen is used as the coolant for the thermoplastic plate in the erase process. This consists of reheating the thermoplastic to releive it of the surface contour variation and to produce a ripple free surface. Upon cooling, the plate is ready to be used again in the formation of a hologram.

1.2.6 Experimental Procedure

A schematic of the holographic interferometer used in this study is shown in Figure 9. It is a standard off axis holographic system. Proper choice of reference to object beam intensity ratio is important for producing the best holograms. With the use of the instant recording device, the quality of the hologram is insensitive to the exposure time. In the real time mode, the test specimen is illuminated in a state

S_1 (say) with coherent light transmitted from the laser via the object wave path (this consists of the beam splitter, a beam exapnder-spatial filter, collimating lens). The corresponding load is $\mathbf{P}_1$ (refer to Figure 10). A hologram is then recorded by exposing the thermoplastic plate positioned at the junction of the reflected light and reference beam. Upon completion of the first exposure the specimen which is continuosly loaded is viewed through a camera attached to a VHS recording system (a VCR and a monitor). The resulting image consists of fringes which are dynamical in nature representing contour maps of the changes, with respect to the state S_1, of the out of plane displacement component w of the stressed specimen. These fringes, together with the load cell reading are recorded. The load cell reading is obtained by focussing the display of the voltmeter, exhibiting the load cell reading, at the position of the circular hole in the plane of the test specimen. With increasing load on the specimen the fringe density becomes high, so that the resolution of the interferogram becomes poor. At this stage a new hologram of the test specimen is made and the above cycle of events is repeated. Thus, finally at the end of each experiment we obtain an interferometric recording of the complete load - out of plane displacement history of the specimen. This sequence of events is shown graphically in Figure 10.

Each of the holographic interference fringe field is related to the change in surface displacement of the specimen under load, by the vector expression

$$n\lambda = \tilde{k}.\tilde{d} \tag{1}$$

where,

n fringe number

λ wavelength of the coherent laser light

$\tilde{k}$ sensitivity vector $(\tilde{i}_2 - \tilde{i}_1)$

$\tilde{d}$ surface displacement vector at point of observation

$\tilde{i}_1$ and $\tilde{i}_2$ are the unit vectors in the illumination and observation directions respectively. In the present experimental setup the diffusely reflective surface of the specimen is oriented normal to the bisector of the angle 2α, between $\tilde{i}_1$ and $\tilde{i}_2$ (Figure 11). Thus, since the sensitivity vector $\tilde{k}$, also points along this bisector, the interferometer senses only the out of plane displacement component w. Equation (1) then becomes

$$n\lambda = 2wcos\alpha$$

$$w = \frac{n\lambda}{2Cos\alpha} \tag{2}$$

In the present experimental setup, the surface normal is 10^0 off the observation direction. With $\lambda = 0.633$ μm, this shows that each fringe represents an out of plane displacement change of 0.321 μm.

A schematic of the present experimental set up is shown in Figure 12. During the entire loading program, the surface of the hole is viewed through a microscope and photographs are taken at various times. A fibre optic cable attached to a high intensity lamp is used to illuminate the hole surface. The interferograms displayed on the TV monitor helps taking these photomicrographs interactively in an efficient manner. Table 2. summarises the test conditions and the results obtained. In this table the last two columns represent normalised "loads" at initiation and failure. Here, "A" is the cross sectional area of the specimen on which the loading is applied and E_{CLT} is the Youngs modulus in the load carrying direction, calculated using *classical laminated plate theory.* In the second column, "AS" for example refers to type "A", small. The ply properties used are given in Table 1.

The interferometric data reveal the changes in the w displacement component. These changes may be the manifestations of internal damage. Thus, some specimen were loaded to a post initiation level but were unloaded prior to catastrophic failure. The unloaded specimen were sectioned in the region of stress concentration and were examined under an optical microscope. In the following section the results obtained from *Interferometry, Photomicrography* and *Interior damage studies* are presented.

1.3 Results and Discussion

In this section the results obtained in the experimental program are presented and discussed. The interferometric data are presented only in the immediate neighbourhood of the hole. The photomicrographs are only captured on one side of the hole surface as indicated in Figure 13. The horizontal shiny stripes appearing on the photomicrographs are 0^0 layers while vertical lines are scribe marks for purposes of reference. The top edge of the hole surface appearing in the photomicrographs correspond to the side on which the interferometry is carried out. Only a part of the hole surface appearing in the photomicrographs is in focus, as this surface is viewed at an oblique angle through the microscope.

We now consider the different stages of failure as exhibited by the interferometric results and substantiated by the photomicrographs. In the pre-damaged situation an increase in the load on the specimen results in a uniform pattern of fringes. These fringes are a few in number and correspond to the thickness changes due to the poisson ratio effect, but coupled with some rigid body motion and/or slight bending. The rigid body motion and the bending cannot be totally avoided in a compression test. The slight bending may be the result of any initial imperfection in the specimen. Added to this we realise the high sensitivity of the technique which is a function of the wave length of the laser light. (displacement changes as small as 0.316 μm can be detected). In the discussion to follow we first consider the responses of Type A and Type B specimen separately and summarise the common features of the failure process at the end.

Type B specimen

This type of specimen is one in which there are a fewer number of 0^0 plies (25%). Figure 14. shows a series of interferometric patterns, which correspond to the first instance at which internal damage was detected. The numbers below each picture represent the load in *lbf* ($\times$ 4.448 N) corresponding to each frame, while P_h indicates the load at which the hologram was made (*Reference load*). Notice the highly localised fringe cluster adjacent to the hole edge at approximately 90^0 to the loading direction. When any form of internal damage occurs that manifests itself as a localised perturbation in the normal displacement component w the resulting interferometric patterns display this event as shown in the figure. A view of the hole surface corresponding to this fringe pattern is shown in frame 2 of Figure 15. Notice the damage to the midplane 0^0 plies which appear as a black spot. Adjacent to this spot is a delamination crack. Inspection of the photomicrographs prior to this event revealed no damage to the hole surface. In all tests it was revealed that *always* a *perturbation* in the *Interferometric data* corresponded to 0^0 *ply damage at the hole surface.* We interpret this interferometric pattern as a localised bulging of the surface just above the damage site. This localised damage to the 0^0 plies is found to be the triggering of extensive delamination cracking and buckling. The above sequence of events is consistently observed in all of the Type B specimen. At this stage we point out that when we refer to damage we mean the destruction to the specimen caused by the application of mechanical load as picked up on the interferograms. The interferograms corresponding to the initiation event reveal the displacements within the damage zone to be increasing with increasing load. This is clear by noting a sharp increase in the fringe density within the damage zone as loading proceeds. Subsequent to the initiation, the remaining 0^0 layers undergo failure while delaminations are seen to appear between various ply interfaces. An inspection of the sequence of photomicrographs in Figure 15 shows this. The delaminations undergo a stage of slow growth as shown in the next set of interferometric patterns (Figure 16). Here the reference state corresponds to a load P_h = 35,760 *lbf* (159 kN) while the three frames span a load increase, ΔP of 390 *lbf*(1.73 kN). The displacement patterns corresponding to this figure are shown in Figure 17. Here the displacements are measured with respect to displacements in areas remote from the hole edge. The origin of the axes is placed at the edge of the hole as indicated. The X and Y axes are scaled while the vertical axes representing Δw is 1:1. The fringe patterns reveal the displacements to be growing faster within the damage zone than the rest of the specimen. Further the damage area is also growing. The corresponding photomicrographs show the extent to which delamination cracking occur. Notice the zero fiber breaks as well as the large (on the order of a ply thickness) mode I type displacements. These observations lead us to beleive that *Delamination Buckling* is the mechanism chiefly responsible for spreading of the damage to the undamaged areas of the plate. Once the delaminated portions reach a sizeable extent an increase in the growth rate is noticed. This is shown in the last series of interferograms (Figure 18). In these the fringe density within the damage zone is very high,so much so, that the resolution of the interferogram within this area is poor. However the manner in which these delaminations grow and respond can be deduced by follwing the fringe development within the damage area. This will be discussed later in the context of Type A specimen. It must be pointed out that playback of the recorded video information displays a continuos transition in the fringe data which enables following the damage progression un-interrupted as opposed to the limited number of frames displayed here. Our discussion is influenced from such a knowledge. The culmination of the last growth event is the complete loss of flexural stiffness of each of the delaminated portions, leading to catastrophic failure. These findings and conclusions are drawn from the consistency with which these failure events occur in all specimen. Figures 19a through d depicts the same scenario of events leading to failure as described (for another specimen with a different geometry).

Next, we turn to a discussion of post experiment microscopic studies. It was felt that the 0^0 ply damage observed in the preceeding section warranted further examination. As such, some specimen were loaded into the post initiation level but unloaded prior to catastrophic failure. In particular the specimen whose interferometric results were discussed earlier, was unloaded near its ultimate failure load and sectioned for further study. An enlarged view of the black spot appearing in the photomicrographs is shown in "A" of Figure 20. Notice that a part of the picture is out of focus. This is because the fibers in that region have jutted out of the plane of the hole surface (plane of the picture). Examination of similar damage to other 0^0 layers revealed the same type of jutout failure. It was also of interest to determine the extent to which the hole surface damage propagated into the interior of the specimen. The laminate was sectioned at different locations as indicated in Figure 21. Magnified views of the 0^0 layers at sections "E" and "D" are shown in Figure 20 & 22. Notice the dark regions showing broken fiber segments scattered at different angles. In "D" an undamaged portion of the midplane 0^0 layer is shown contrasted against a damaged portion which clearly indicates a characteristic pattern. Here we see a V shaped matrix rich area, within which the fibers have undergone rotations. The maximum width of the V shaped zone measures to be approximately 0.3 *mm*. The matrix rich portion in the bottom right hand picture is seen inclined at an angle of 65^0 to the 0^0 fiber direction. These characteristic patterns of failure have collectively been refered to as *Fiber kinking* in the literature.

This type of kinking failure has been observed in other studies dealing with compressive strengths of laminates (see for eaxample [9]-[11]). What still remains as a nagging question is the origin of fiber kinking.

Sectioning beyond cross-section "D" and inspection under the microscope revealed no further damage. Similar inspection to other specimen loaded to levels just prior to catastrophic failure revealed that the damage zone was contained within one hole radius.

Planform views of the damaged midplane 0^0 layer as obtained by mechanical polishing is shown in (a) of Figure 23. Here we note the matrix rich damage zone which measures in width to approximately 70 fiber diameters (0.5 mm). Closer examination of the edge of the damage zone revealed that the fibers had undergone rotation in the plane of the picture. Thus, in this zone the fibers have not only undergone rotations in the XY plane, but also in the XZ plane as indicated by the sectioning studies earlier. Similar results were obtained from the deplying study which consists of heating the damaged samples to about 600^0 F and removing ply by ply to observe internal damage. Shown in Figure 24a is a C-scan of a specimen loaded upto about 90% of its failure load. This scan is a planform view of the integrated through thickness damage. Here we note the clear resemblence between the shape of the damaged area and the portion of the interferometric patterns that contain a very high fringe density.

Type A specimen

These specimen have a higher number of 0^0 layers (42%) than Type B. Figure 25 shows a series of interferograms corresponding to the first instance at which a perturbation in the fringe pattern occured. A sharp localised cluster of fringes is seen formed at the edge of the hole which spreads very rapidly with a small increase in load. It is seen that the area in which the fringes are unresolvable extends out to about one hole radius from the hole edge. The corresponding photomicrograph is shown in frame 2 of Figure 26 (corresponds to P = 28990 lbf[129 kN]). Here a single 0^0 ply failure remote from the front surface of the specimen is visible. The interferometer detects this internal damage. A fringe count of frame 5 in Figure 25 reveals a w displacement change of approximately 6-10 μm, at the hole edge, perpendicular to the direction of applied load. This displacement is on the order of a fiber diameter (7 μm). In the last frame of this sequence, the fringe density at the hole edge is too high, precluding any possibility of a fringe count. With increasing load surface buckle formation on the other edge of the hole approximately at 90^0 to the loading direction is found to occur. This event is shown in the series of interferograms that are displayed in Figure 27. The buckle formation occurs very rapidly and as indicated in the figure the duration between the last two frames is 0.1 seconds. Inspection of the photomicrographs shown in Figure 26 reveal the manner in which progressively the remaining zero layers fail with increasing load. A picture of the damaged, unloaded specimen is shown in the last frame of Figure 26. A similar pattern of failure is displayed by several other specimen and a sequence of such photomicrographs is shown in Figure 28. Here the first 0^0 fiber failure occurs at 27890 lbf (124 kN) close to the front edge of the specimen and is shown in the third frame of the montage of pictures. The fourth frame corresponding to several zero ply failure and the formation of a *surface buckle* is designated the time T=0 seconds. The subsequent progression of failure leading to catastrophic failure is shown in the next series of frames, with the final disintegration of the specimen occuring within about one minute subsequent to frame 4. Notice the damage to all 0^0 fiber layers and the formation of surface buckles on both surfaces of the specimen.

In many of the interferometric sequences discussed so far it was found that fringe resolvability was poor close to the hole surface. This is because the displayed pictures which are shot off of a TV monitor screen, are recorded using a standard video camera which is incapable of resolving all of the information stored in the thermoplastic plate. Thus, some picture quality is lost in this process. To check the regions of high fringe density we modified the recording procedure by placing a beam splitter. behind the thermoplastic plate and taking pictures of the interferograms using a 35 mm SLR camera, while still recording on the VCR. A sequence of such interferograms showing the final stages of failure of a Type A specimen is shown in Figure 29. The fringes on the top half of the pictures display a continuous variation in w. Further, the fringe gradient is seen to rapidly decrease away from the hole edge. A fringe count of frame 3 reveals a w displacement change at the hole edge of 10 μm. These pictures display a superior resolution. However,to adopt this method for the entire duration of a test would be cost ineffective. What is important here, is to compare the fringe patterns, to those taken off of the TV monitor. It is seen that the areas in which the fringes were unresolvable earlier could be smoothly extrapolated from the areas in which the fringes are resolvable. We also see that a surface buckle is already formed on the bottom half of the specimen. This damage is contained within a distance of approximately half a radius of the hole. The sequence 1-4 depicts the formation of the buckle on the top half of the specimen which is found to be the last event prior to catastrophic failure. The pictures were taken with an exposure time of approximately 1 second with the duration between frames approximately 2-3 seconds.

Bearing in mind the information obtained from the surfaces of the specimen, we now turn to a discussion of post experiment sectioning studies. Shown in Figure 24b is a C-scan of the lower half of a typical damaged specimen. Notice the extent of the damage area which is contained within about a hole radius. In Figure 30a we show a typical section through this damaged area. Here the interior 0^0 layers show several inclined narrow zones of fiber breaks, identified as *Fiber Kink bands.* A typical complimentary kink band is shown in Figure 30b. We note here a kink band inclination of 65^0 to the load carrying direction. The lengths of the fibers in the inclined zone measures to 50-84 μm. More importantly it is pointed out that the region between the inclined zone appears undamaged and oriented parrallel to the fiber direction. The geometry of the kink band is summarised in Figure 31. In this figure we also include the notation used to describe a typical kink band from ref. 10. In that study carbon fiber bundles of width $\approx$ 400 μm oriented in three orthogonal directions were set in a Graphite matrix and subjected to localised impact. Post-experimental examination revealed typical *kink orientation* angles α of 45^0 - 60^0 and kink boundary orientation β obeying $\beta \approx \frac{\alpha}{2}$ for broad($\frac{l}{d} \geq 0.1$) kinks. Here β is measured from the *perpendicular* to the fiber direction. For narrow kinks β was found to increase and α random. Corresponding results in our study which fall into the category $\frac{l}{d} \geq 0.1$ indicate $\beta \approx 25^0 - 30^0$ and $\alpha \approx 15^0 - 30^0$. However, no definite trend between α and β can be established. One difference in the present case is that the specimen are loaded well into a post damaged state as opposed to being unloaded just after initial damage.

It was seen earlier that the outermost layers of the laminate that underwent large displacements in the buckling process suffered fiber breaks. A magnified view of such a fiber break is shown in Figure 30(c). It was of interest to examine the propagation of the initial fiber kinking failure into the interior of the specimen. This was done by sectioning at several positions and following the damage of a typical 0^0 layer. The results thus obtained are shown in Figure 32. Notice that the appearance of the kink is unaltered at several different cross sections. Further, the same type of geometry as found before is seen to prevail with an area of undamaged fibers between two inclined bands of damaged fibers which have undergone rotation in the XZ plane. The lengths of the fibers in the damage zone are comparable to those seen before. A planform view of such a damaged 0^0 layer is shown in Figure 23b and c. The damage zone width is approximately 0.27 mm (38 fiber diameters). Here we note the fiber jutout failure at the edge of the hole. The damage zone appears dark as the fibers in this area which are broken and kinked out of plane were polished off during preparation of the specimen for microscopic examination. Finally in Figure 33 we show the outer layer delamination crack at two different cross-sections.

Summary of common features of failure

In this section we summarise the results presented so far and try to identify features that are common to both types of laminates.

In both types the failure is initiated by a 0^0 fiber failure at the hole edge approximately at right angles to the loading direction. In type A, with increasing load more 0^0 fiber failure is seen to occur with simultaneous surface delamination buckling. These events occur very close to the catastrophic failure load. In type B, subsequent to 0^0 fiber failure which occurs at around 75% of the ultimate failure load, extensive delamination cracking is observed, with the outermost delaminated sections undergoing buckling. Photomicrographs typical of these two types are contrasted in Figure 34. In both types the delaminations are seen to grow with increasing load. *Delamination Buckling* is found to be the mechanism responsible for the spreading of the damage. When the delaminated portions grow to a critical size, approximately on the order of one hole radius the specimen fails catastrophically.

The mechanics of the 0^0 fiber failure, which shows up at the hole edge and captured by the interferometer is found to be a localised microbuckling/fiber kinking. The question to be addressed is the process by which such kinks form. Information regarding fiber kinking published elsewhere and at present have been obtained once the damage has taken place and the structure loaded into a post-damaged state. Qualitative information regarding the pre damaged state, from the interior of the structure, is difficult to obtain as these systems are opaque. However, the present experimental results lead us to beleive that a *possible* mechanism culminating in fiber kinking is *elastic buckling* of the fibers.

Damage patterns typical of those observed so far are shown in Figure 35. A 3-D view of the damage to a 0^0 ply is summarised in Figure 36. This 0^0 ply microbuckling/kinking which occurs both, in plane (XY) as well as out of plane (XZ), is found to persist well into the interior of the specimen. It is conceivable then, that this type of failure originates at the edge of the hole and propagates into the interior of the specimen, causing a narrow zone within the 0^0 plies to loose structural integrity. Continuous viewing of the recorded videotapes, shows the surface manifestation of this event as a well defined cluster of fringes originating at the hole edge and propagating rapidly away from the hole. The origination of fiber kinking at a free edge and its subsequent propagation into the interior of the structure has been reported before. We cite here the of work of Chaplin [9] and Hahn et al [11].

1.4 Conclusions

In an attempt to understand the mechanisms responsible for the initiation and spreading of damage in composite laminates containing a cutout we have carried out a detailed experimental investigation and presented qualitative and quantitative results. The damage is found to initiate by a combination of *Fiber microbuckling/ kinking*. *Delamination Buckling* is found to be the mechanism by which the damage spreads away from the hole at 90^0 to the loading direction. When the delaminations reach a critical state the plate fails catastrophically. These events which are consistently observed, can form the basis for the formulation of simple mechanics models to highlight the various stages of failure.

Acknowledgements

The authors appreciate the support and interest of Dr. James Starnes. *jr* of NASA Langley research center.

1.5 References

1). Starnes J. and Williams J.G. - Failure characteristics of Gr/Epoxy structural components loaded in compression . NASA TM 84552, Sept. '82.

2). Rhodes M., Mikulas M. and McGowan P. - Effect of orthotropic properties and panel width on the compression strength of Gr/Epoxy laminates with holes, AIAA paper No. 82-0749.

3). Shuart M.J and Williams J.G. - Compression behaviour of [+45/-45] dominated laminates with a circular hole or impact damage . *AIAA journal*, vol. 24, No. 1, p 115, Jan '86.

4). Knauss J., Starnes J. and Henneke E. - The compressive failure of Gr/Epoxy plates with circular holes . NASA CR 157115, N78-24295, 1978.

5). Mikulas M. - Failure prediction techniques for compression loaded composite laminates . NASA CP 2142, 1980.

6). Babcock C.D. and Waas A.M. - Effect of stress concentrations in composite structures . GALCIT SM Report 85-12.

7). Rosen B.W. - Mechanics of composite strengthening ., *Fiber composite materials*, Am.soc. for Metals seminar, 1965.

8). Schuerch H. - Prediction of compressive strength in uni-axial Boron fiber -metal matrix composite materials , *AIAA journal*, Jan. 1966.

9). Chaplin C.R. - Compressive fracture in uni-directional glass reinforced plastics. , *J. of Mat.Science*, 12, p347-352, 1977.

10). Evans A. and Adler A. - Kinking as a mode of structural degradation in Carbon fiber composites ,*Acta Metallurgica*, vol. 26, pp725-738, 1977.

11). Hahn H. and Williams J.G. - Compression failure mechanisms in unidirectional composites , NASA TM 85834, Aug 1984.

12.) Budiansky B. - Micromechanics , *Computers & Structures*, vol. 16, No.1-4, p3-12, 1983.

13.) Chai H. - Growth of impact damage in compressively loaded laminates, P.hD thesis, Caltech, 1982

14.) Vest C.M. - Holographic Interferometry , Wiley, 1979.

Table 1.- Material Properties for T300/BP 907 Graphite/Epoxy

Lay Up : $(+45/-45/0/0/+45/-45/0/0/+45/-45/0/90)_{2S}$

<u>Nominal Ply Properties</u>

Longitudinal Modulus,	E_1	= 111 Gpa
Transverse Modulus,	E_2	= 13 Gpa
Shear Modulus,	G_{12}	= 6.4 Gpa
Major Poisson's ratio,	ν	= 0.38
Ply thickness		= 0.16 mm

<u>Laminate Stiffness Parameters</u>

Dimension: A_{ij}: $10^6 \times$ lbf/in. (=0.176 GN/m)

D_{ij}: $10^3 \times$ lbf-in. (1.13×10^{-11} N-m)

$i,j = 1,2,6$

$$\begin{bmatrix} N_x \\ N_y \\ N_{xy} \\ M_x \\ M_y \\ M_{xy} \end{bmatrix} = \left[\begin{array}{ccc|ccc} 2.891 & 0.689 & 0.00 & & & \\ & 1.484 & 0.00 & & 0 & \\ & & 0.723 & & & \\ \hline & & & 20.9 & 5.376 & 0.255 \\ & 0 & & & 9.688 & 0.255 \\ & & & & & 5.801 \end{array}\right] \begin{bmatrix} \partial u/\partial x \\ \partial v/\partial y \\ \partial v/\partial x + \partial u/\partial y \\ -\partial^2 w/\partial x^2 \\ -\partial^2 w/\partial y^2 \\ -2\partial^2 w/\partial x \partial y \end{bmatrix}$$

TABLE 2. Test Results

Spec.	Type/Size	Hole	Thickness (mm)	Initiation P_I (kN)	Failure P_f (kN)	$\frac{P_I}{AE_{CLT}}$ %	$\frac{P_f}{AE_{CLT}}$ %
TB1	AS	2.54cm(1")	7.51	126 (28400lbf)	127 (28500)*	0.38	0.38
TB2	AS	"	7.51	124 (27930)	125 (28100)*	0.37	0.37
TB10	AS	"	7.53	124 (27890)	127 (28550)	0.37	0.38
TB12	AS	"	7.53	125 (28100)	127 (28450)	0.37	0.38
TB7	BS	"	7.51	64 (14500)	91 (20550)	0.37	0.53
TB13	BS	"	7.47	69 (15600)	90 (20250)	0.41	0.53
TB6	BL	"	7.51	127 (28500)	168 (37800)	0.44	0.59
TB11	BL	"	7.53	123 (27705)	165 (37095)†	0.43	0.57
TB9	BL	"	7.51	119 (26825)	169 (37915)	0.41	0.59
TB14	AS	1.9cm(0.75")	7.47	130 (29150)	142 (31950)	0.39	0.43
TB17	AS	"	7.53	128 (28750)	143 (32200)†	0.38	0.43
TB16	BS	"	7.47	70 (15800)	97 (21850)†	0.41	0.57
TB18	BS	"	7.53	79 (17700)	110 (24800)	0.46	0.64
TB15	AS	1.27cm(0.5")	7.47	152 (34250)	161 (36100)†	0.46	0.48

* —load held constant after initiation
† —maximum load sustained

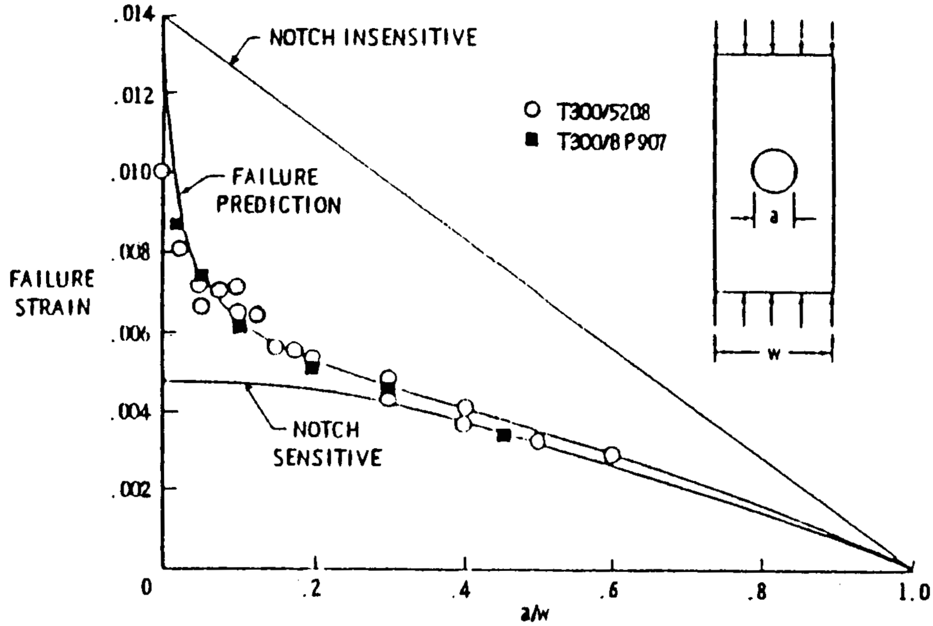

Figure 1. Summary of test results for T300/BP 907, T300/5208 composite plates. w = 13 *cm*. (from Ref. 1)

Figure 2. Experimental set up

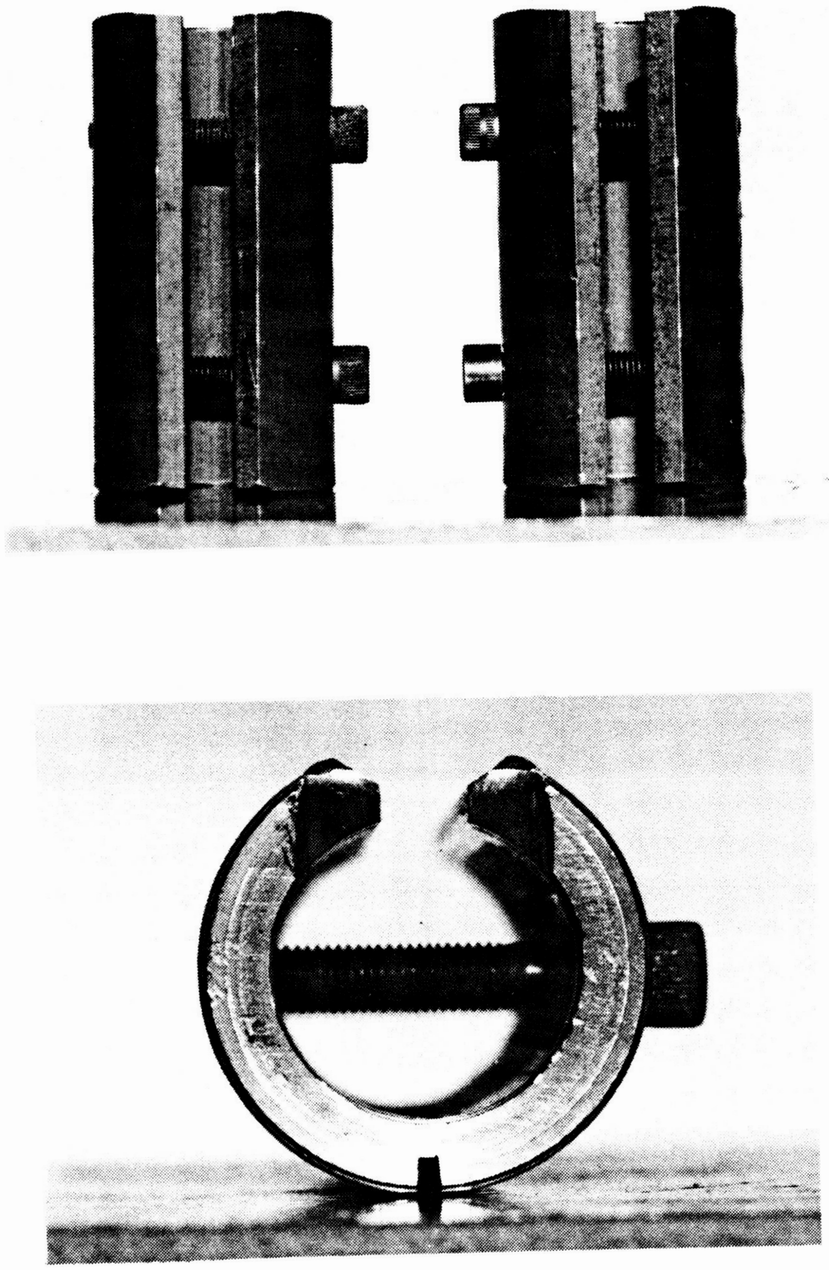

Figure 3. Typical set of edge stiffeners

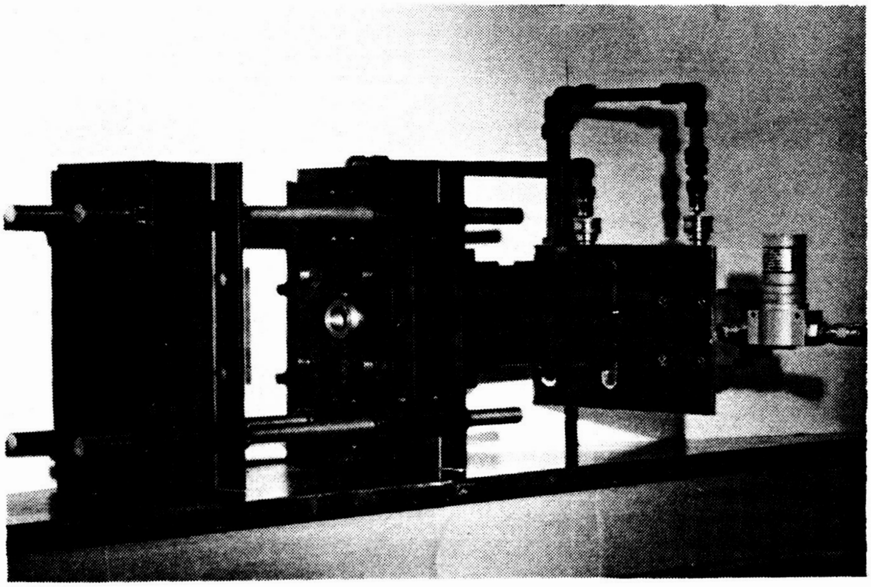

a

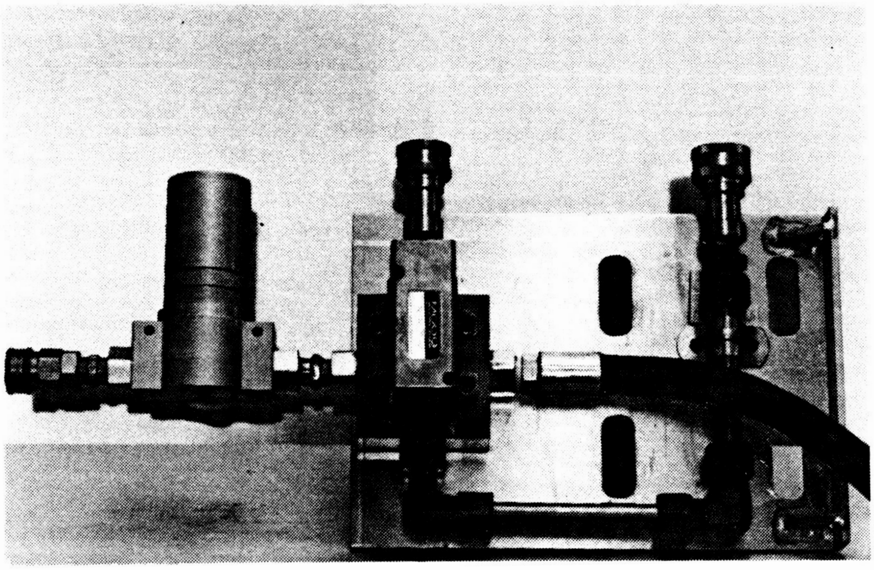

b

Figure 4. (a) Testing machine on optical table
(b) Servo-valve and accessories

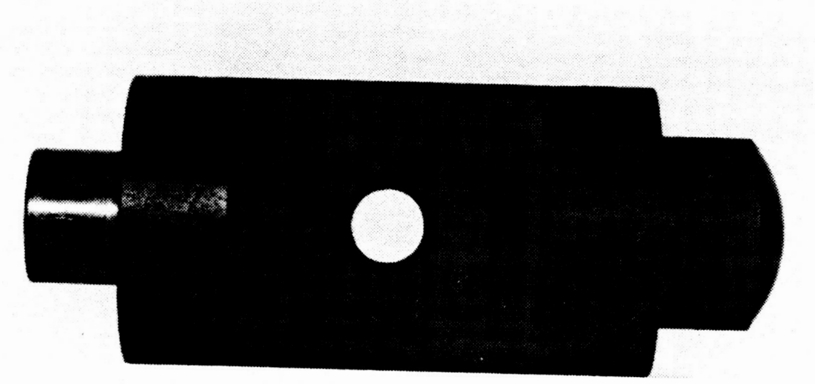

a

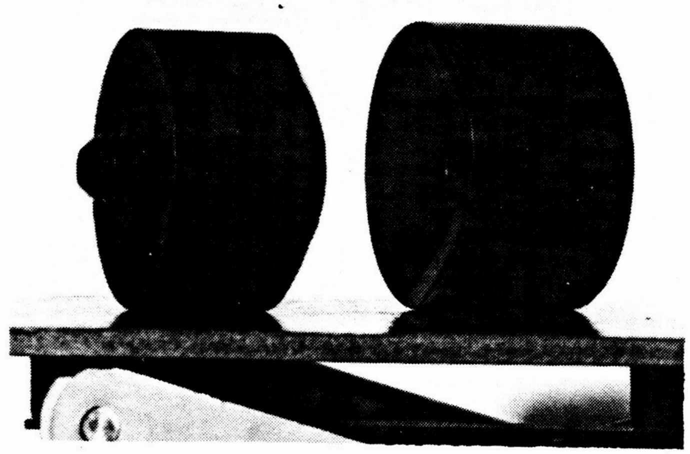

b

Figure 5. (a) Specimen inserted in holders
(b) Ball joint arrangement

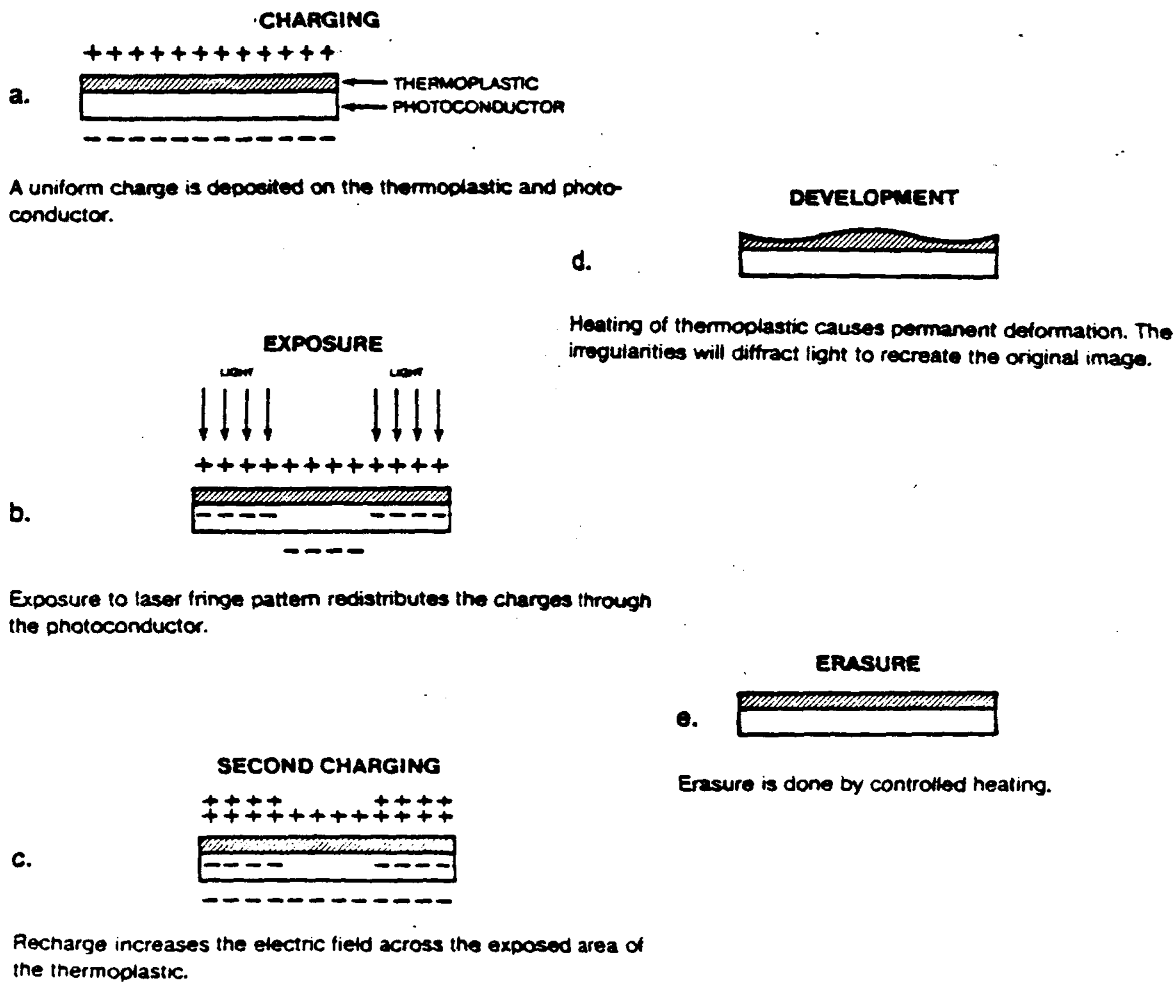

Figure 6. Process of creating a surface-relief hologram on a thermoplastic plate

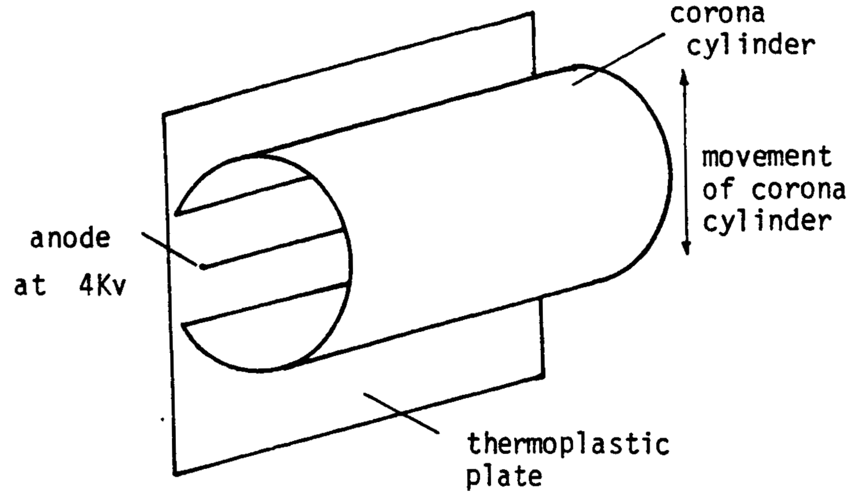

Figure 7. The coronatron deposits a uniform charge on the thermoplastic plate

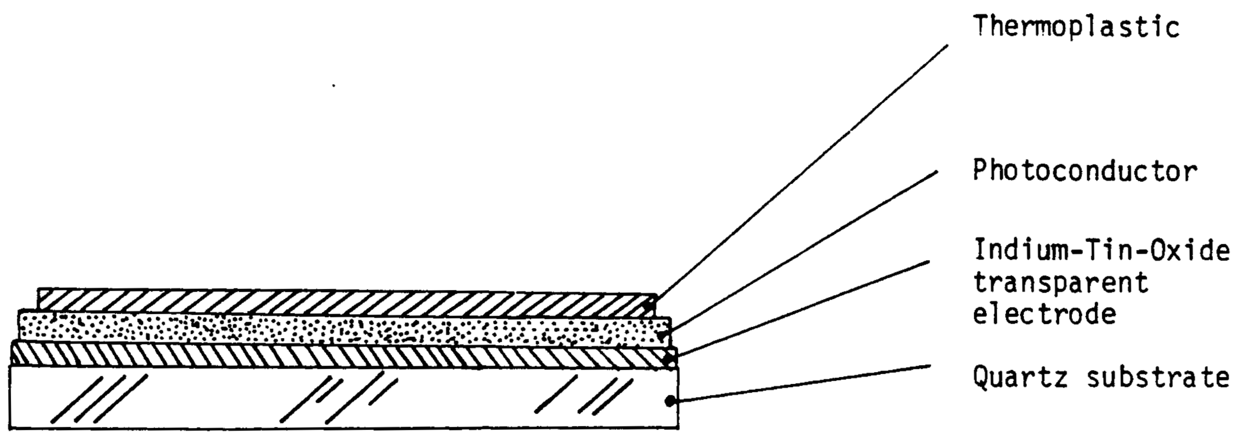

Figure 8. Detailed diagram of thermoplastic plate, showing quartz substrate and transparent electrode

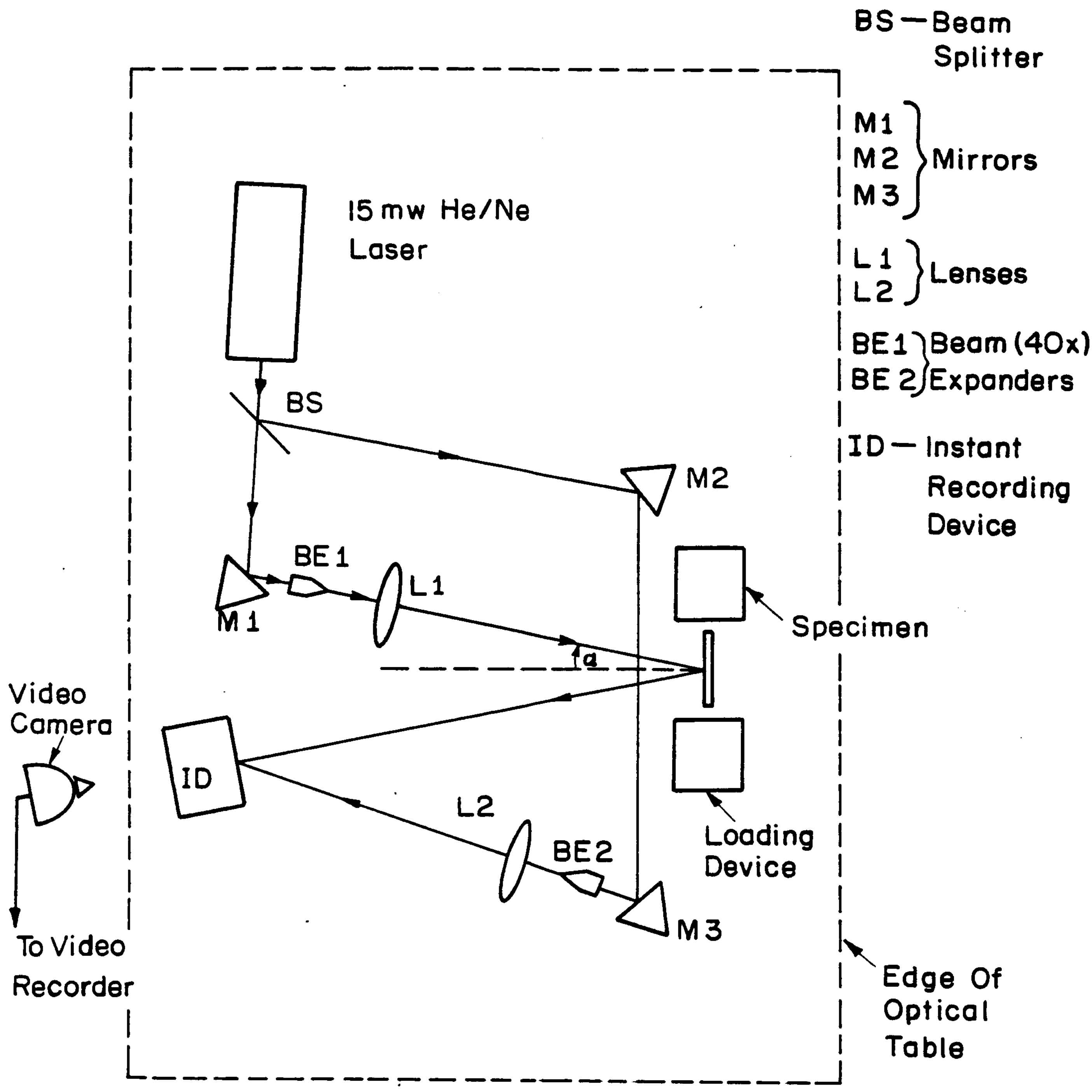

Figure 9. Holographic interferometer

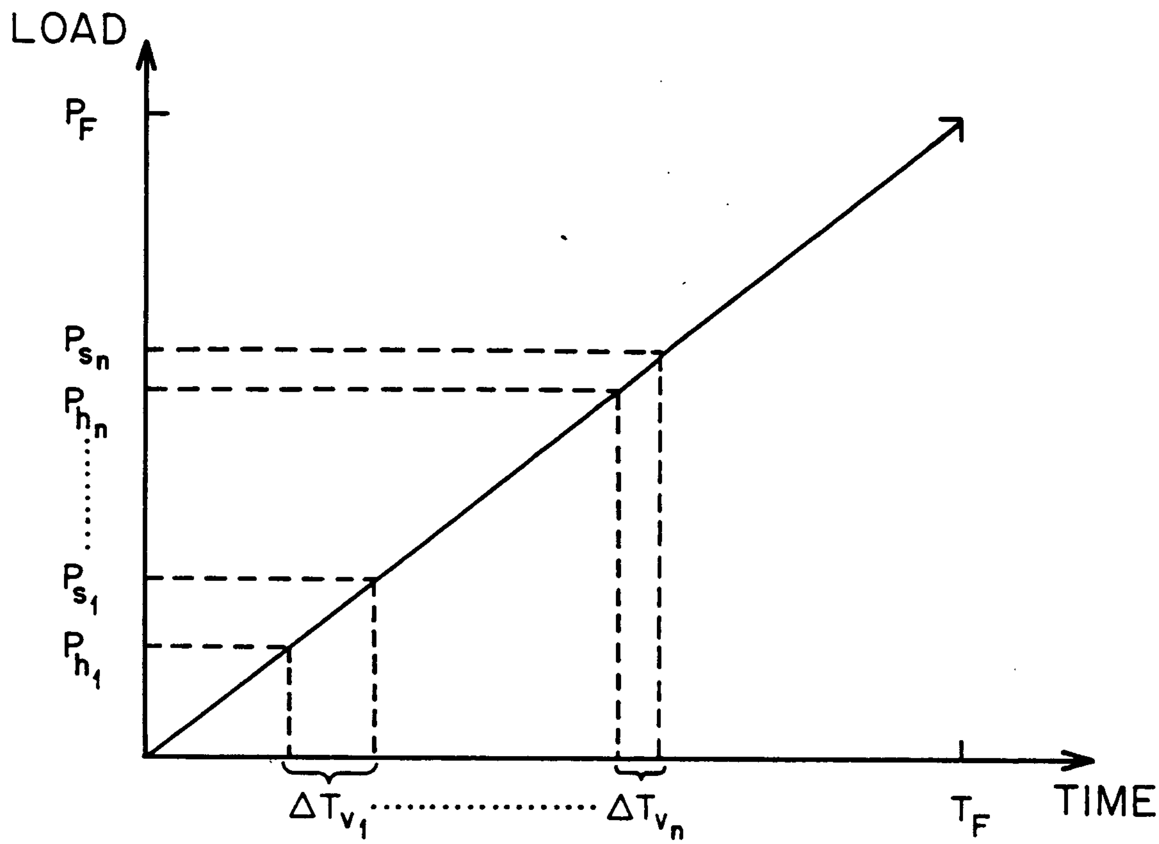

P_h – LOAD AT WHICH HOLOGRAM IS MADE

P_s – LOAD AT WHICH FRINGE RESOLVABILITY IS POOR

ΔT_v – VIEWING DURATION FOR EACH INTERFEROGRAM SEQUENCE

P_F – MAXIMUM LOAD SUSTAINED BY SPECIMEN

T_F – DURATION OF TEST

Figure 10. Experimental procedure for generating interferograms

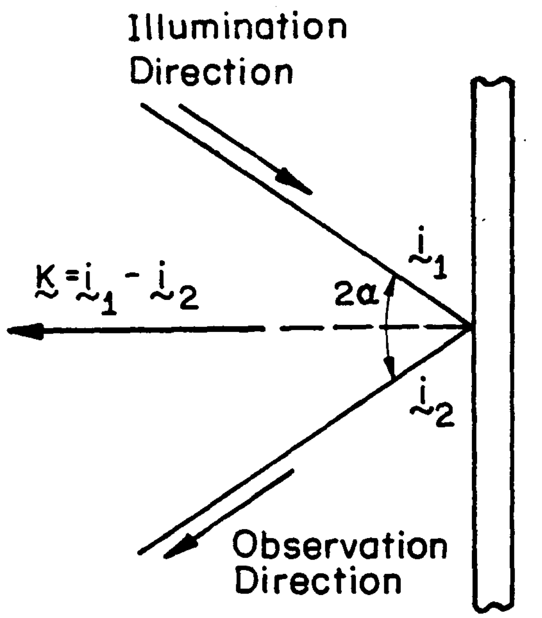

Front Surface
Of Specimen

$\underset{\sim}{i}_1$ Unit Vector In Illumination Direction

$\underset{\sim}{i}_2$ Unit Vector In Observation Direction

$\underset{\sim}{K}$ Sensitivity Vector

$\underset{\sim}{d}$ Displacement Vector

w Component Of Displacement Normal To Plane Of Specimen

$$n\lambda = \underset{\sim}{k} \cdot \underline{d}$$

n Fringe Number

λ Wavelength Of The Coherent Laser Light

Figure 11. Details of interferometer

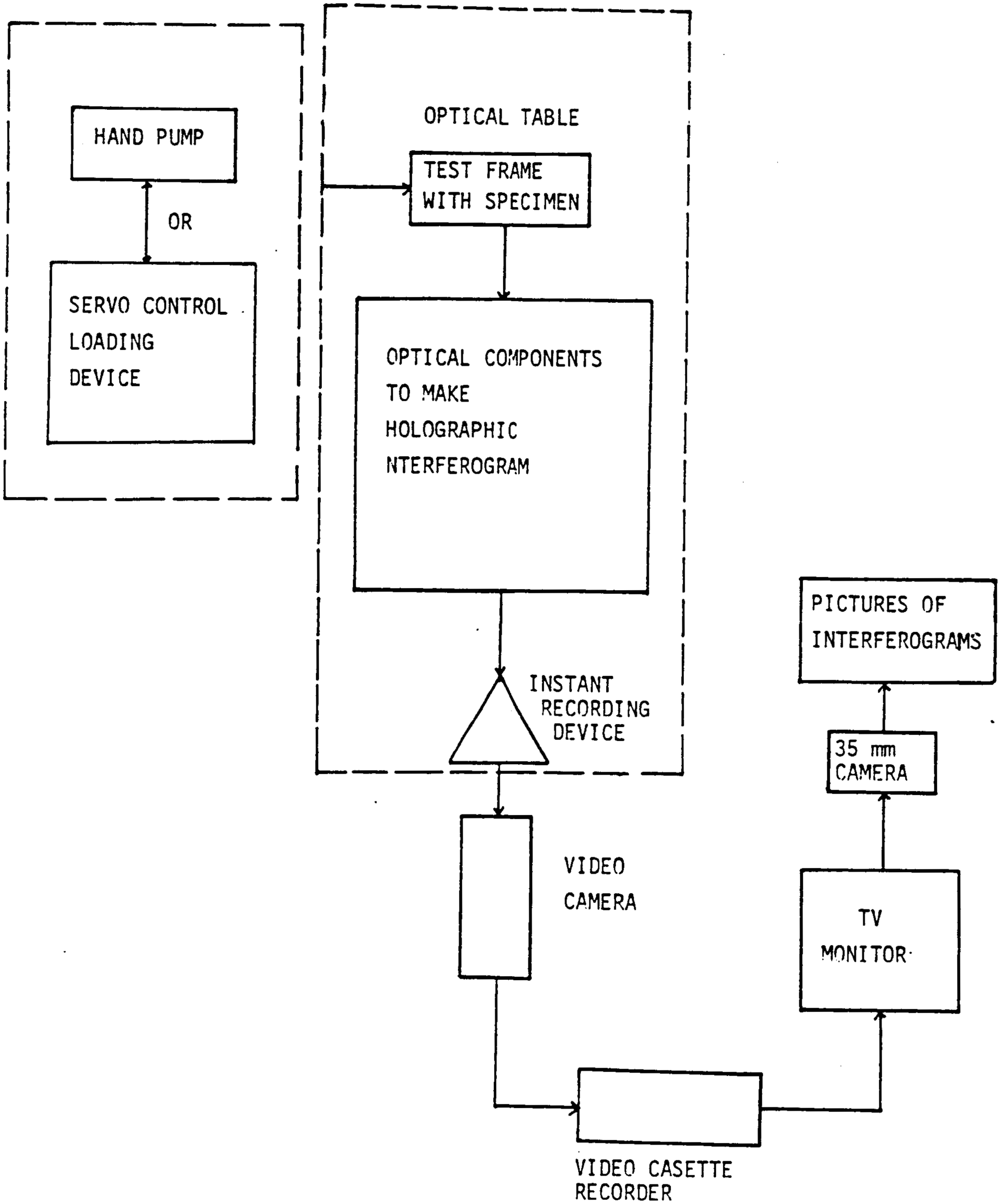

Figure 12. Schematic of experimental set up

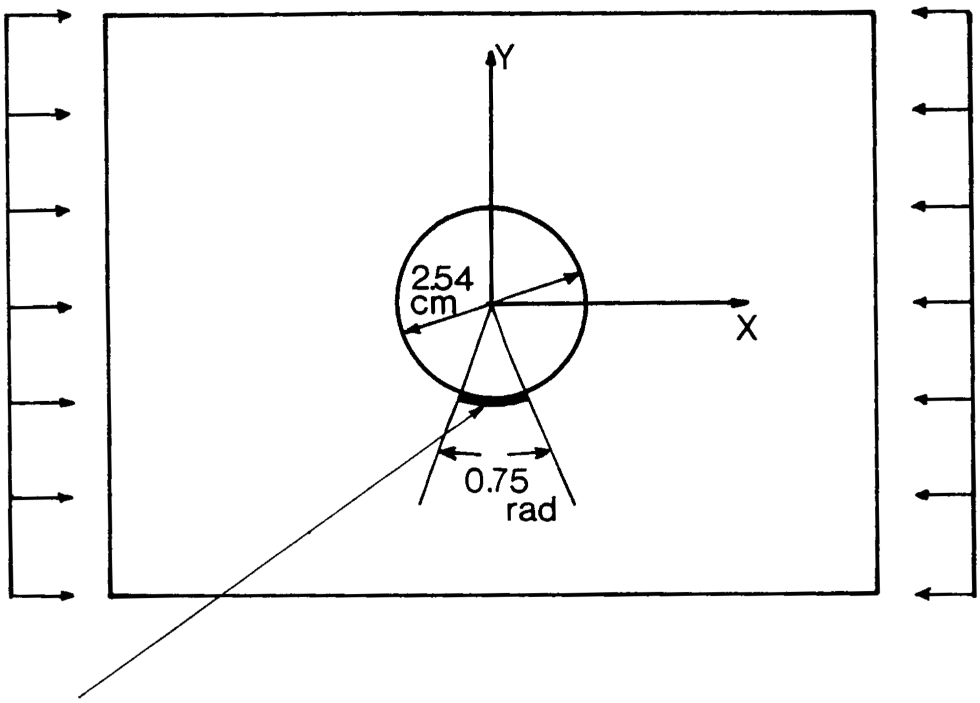

Portion of hole surface in photomicrographs

Figure 13. Photomicrography

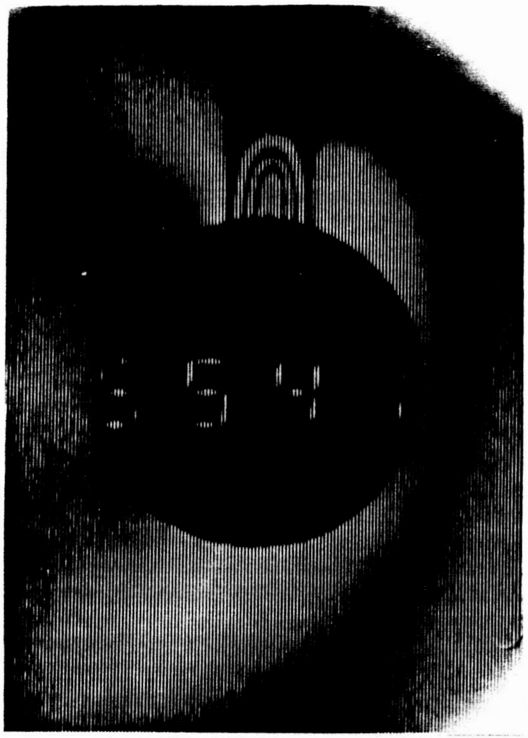

P = 27,705 lbf

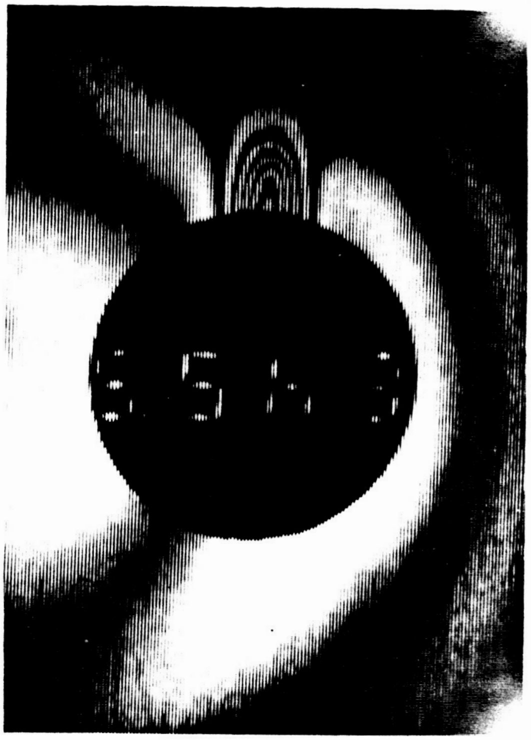

27,815

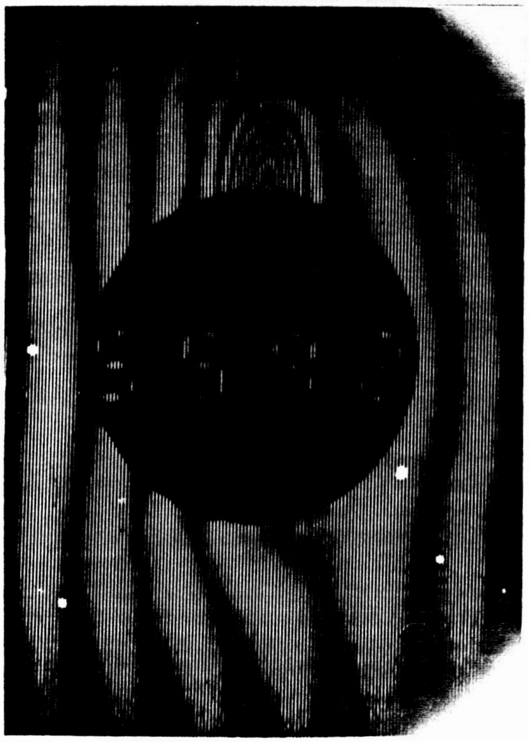

27,960

P_h = 27,700

Figure 14. Initiation of damage.
(Spec. TB 11)

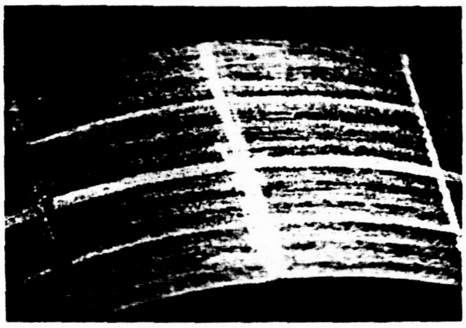

P=15,000 lbf

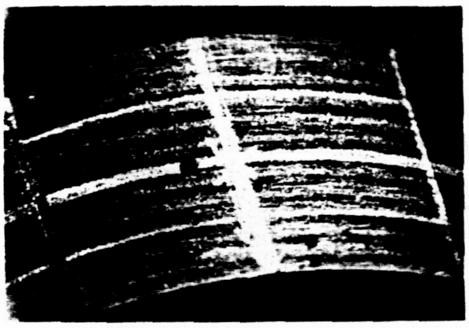

27,700

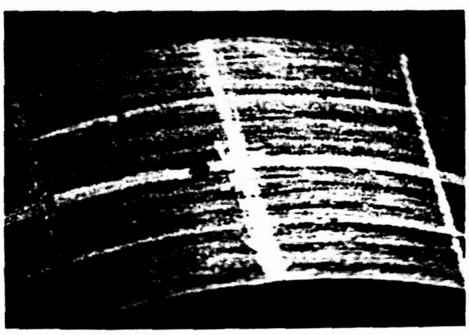

35,770

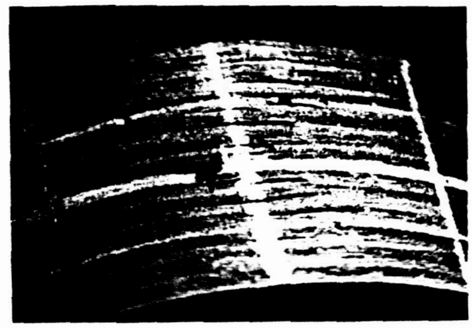

36,980

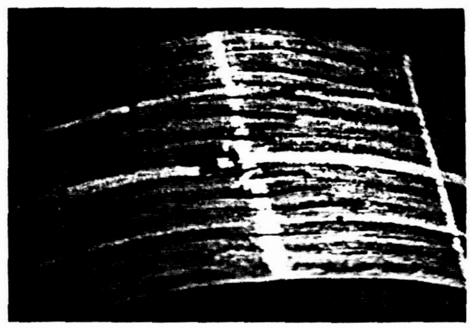

37,100

Figure 15. Hole surface photomicrographs (spec. TB II)

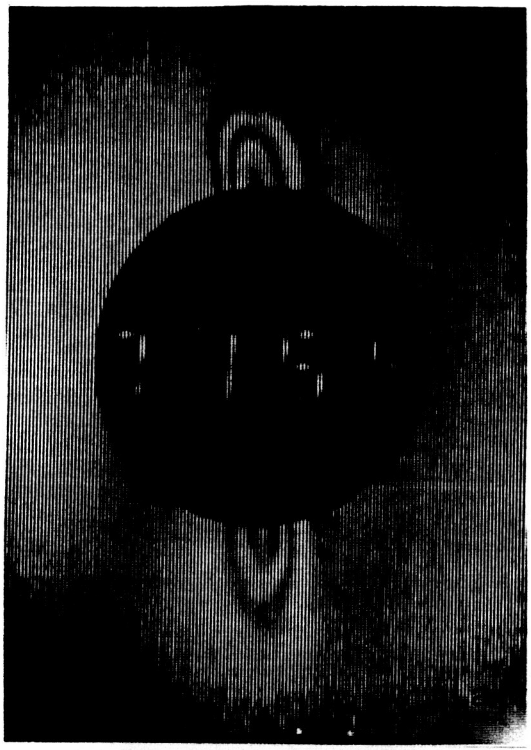

P = 35,770 lbf

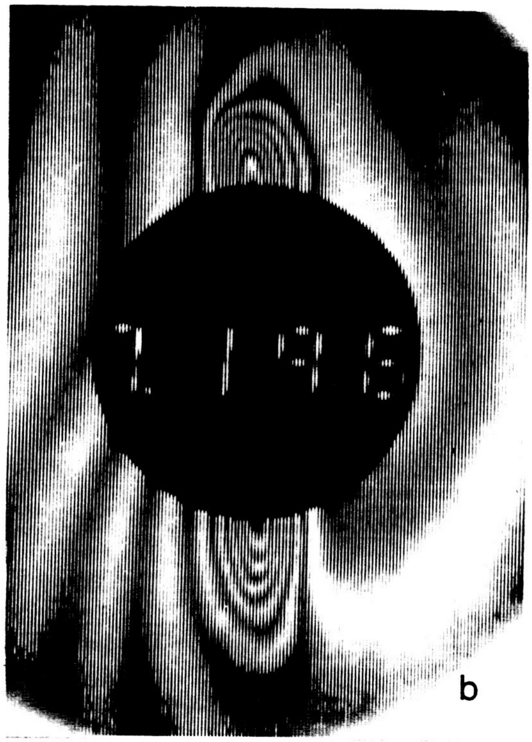

35,980

36,150

P_h = 35,760

Figure 16. Buckling and spreading of delaminated portions. (Spec. TB11)

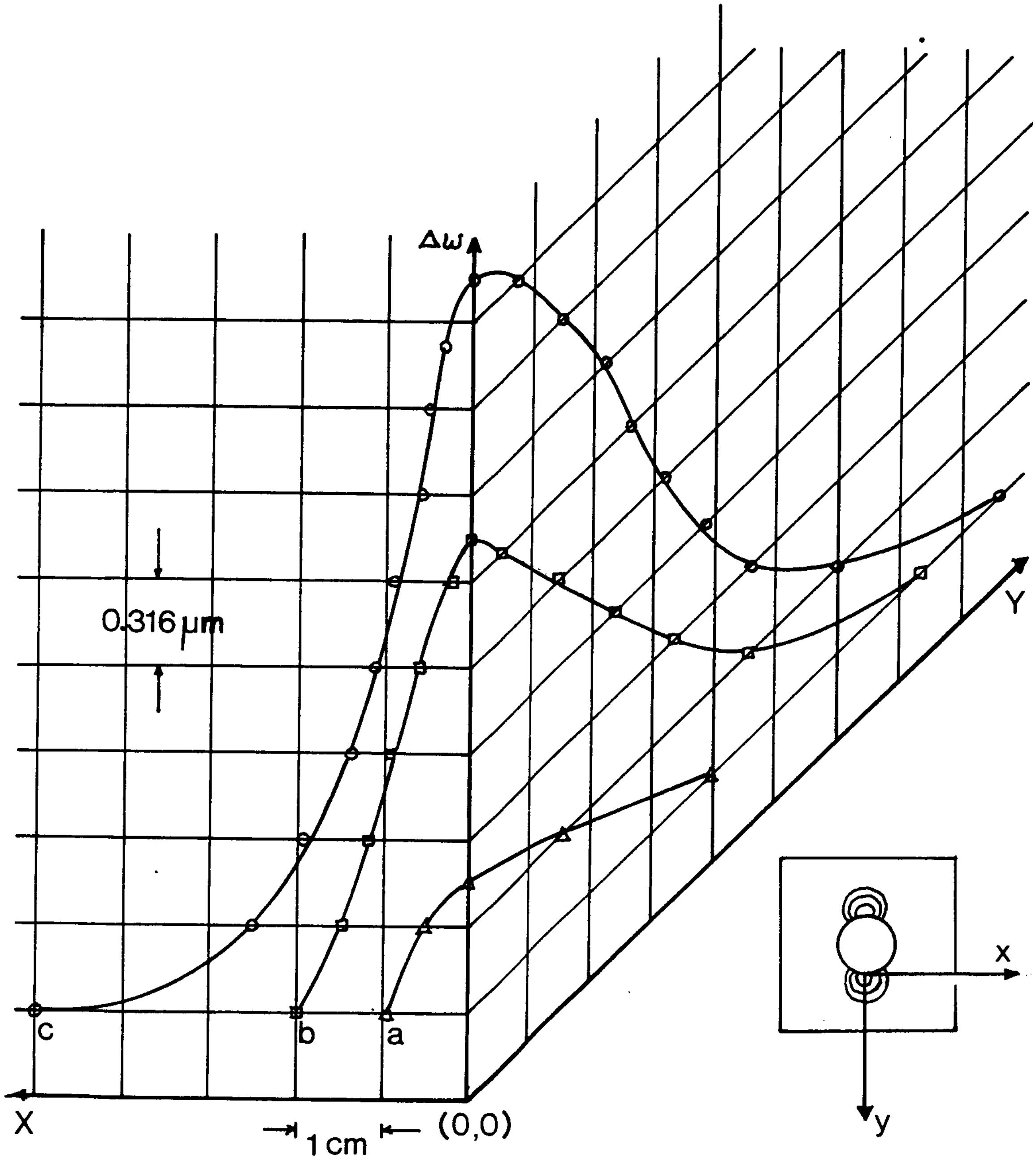

SCALE 1:0.37
(X&Y axes)

Figure 17. Summary of displacement corresponding to Fig.16

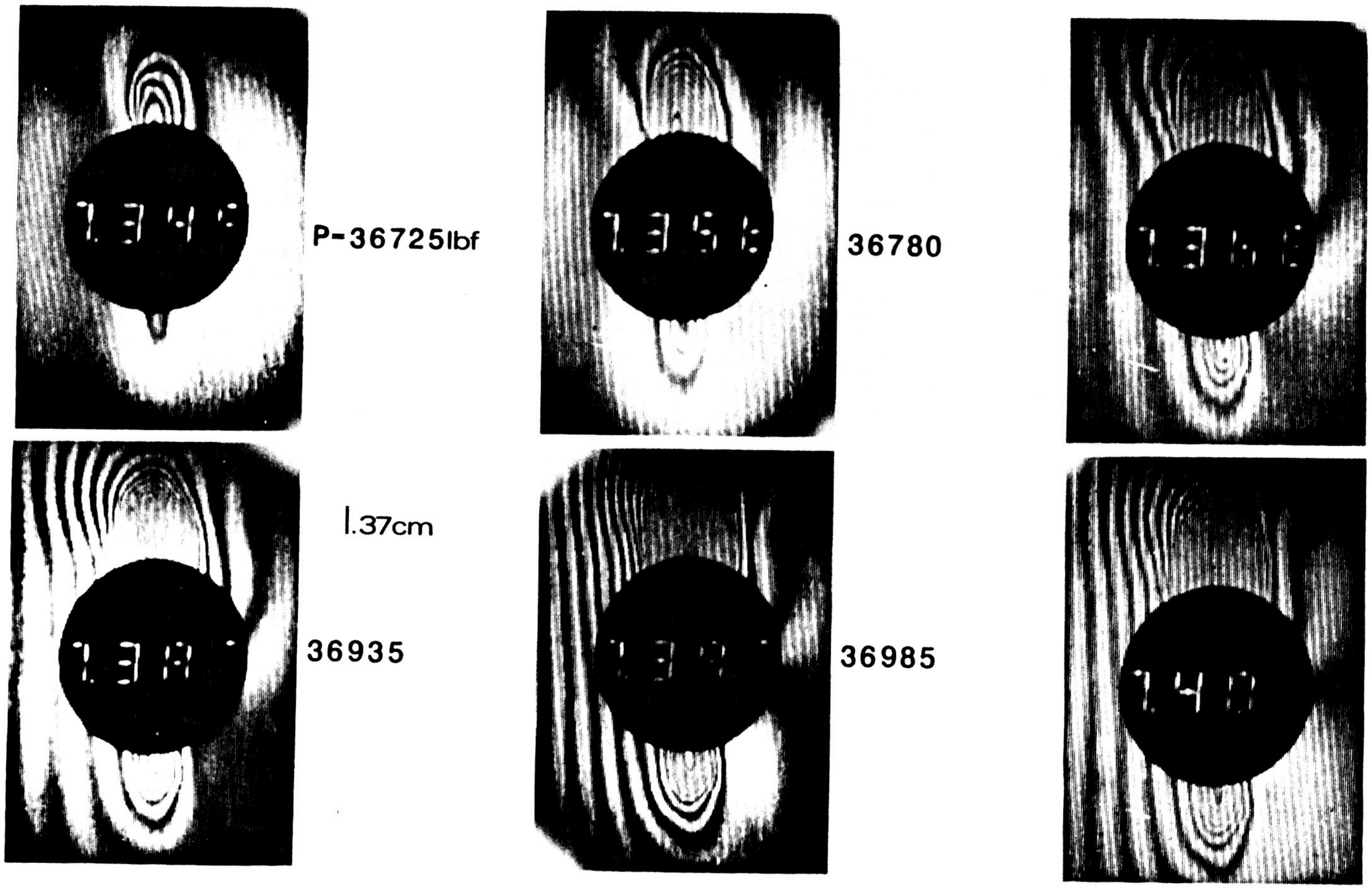

Figure 18. Buckling and spreading of delaminated portions just prior to catastrophic failure.

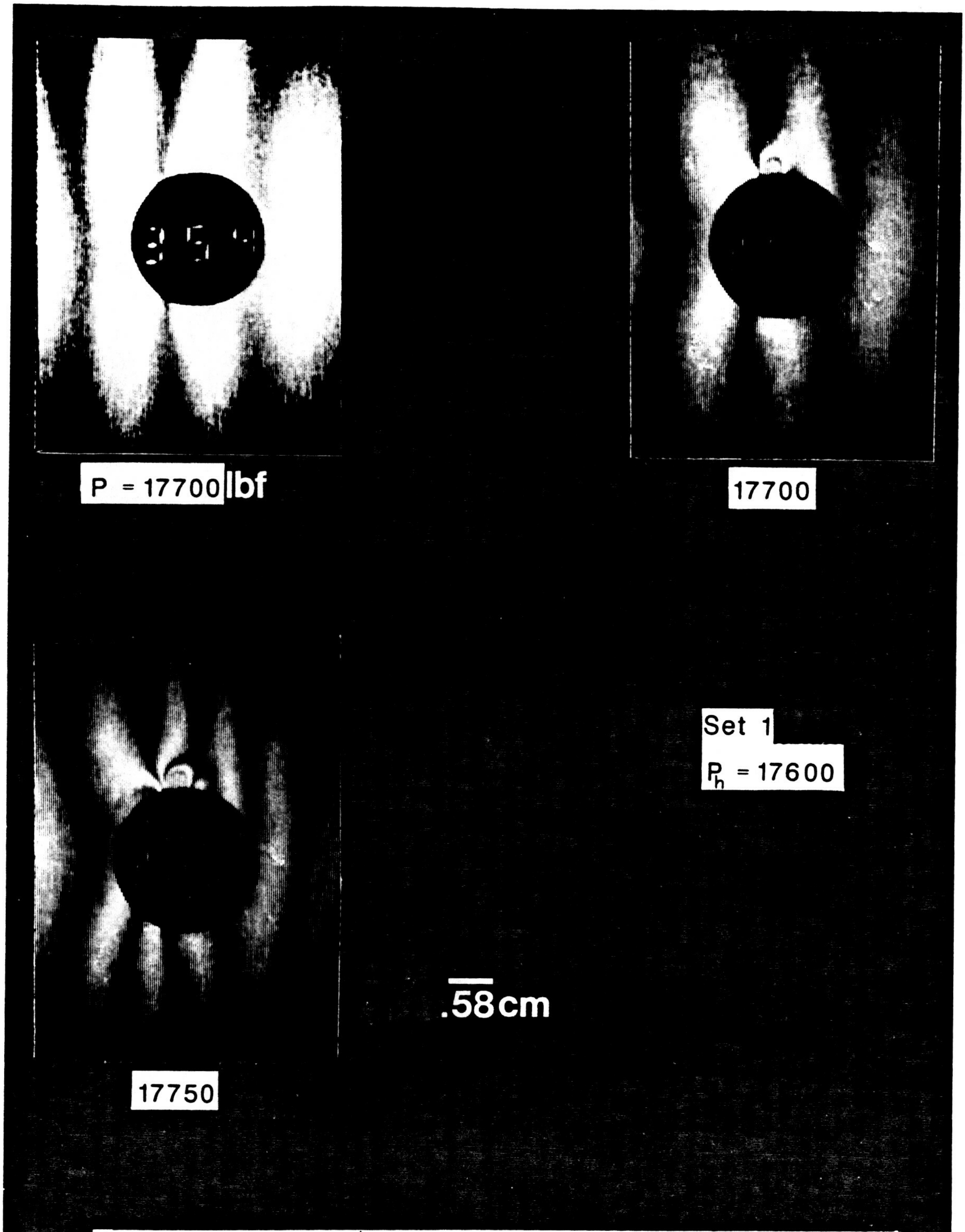

Figure 19a. Fringe pattern at damage initiation.Spec TB18

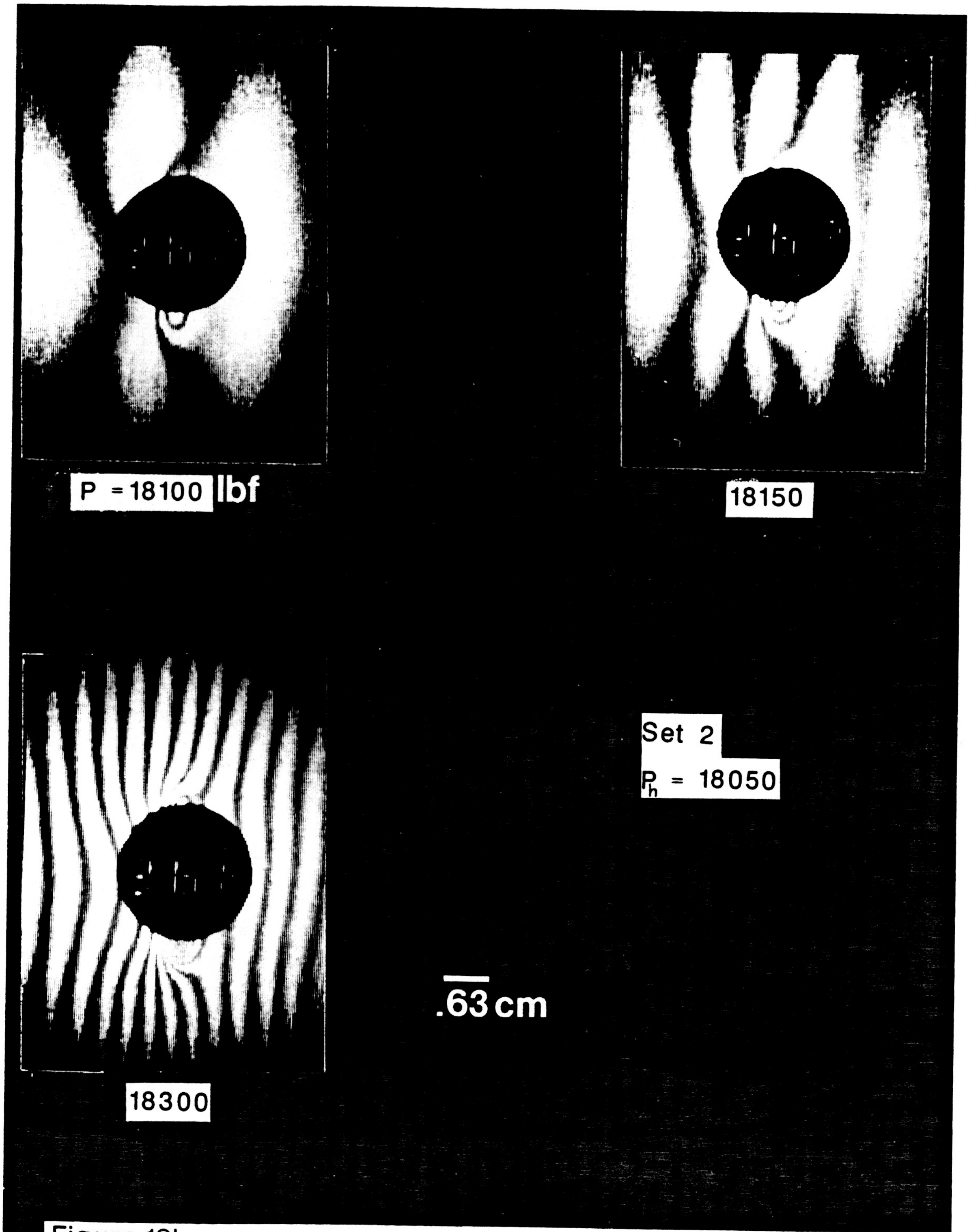

Figure 19b. Response of damaged area with increasing load.

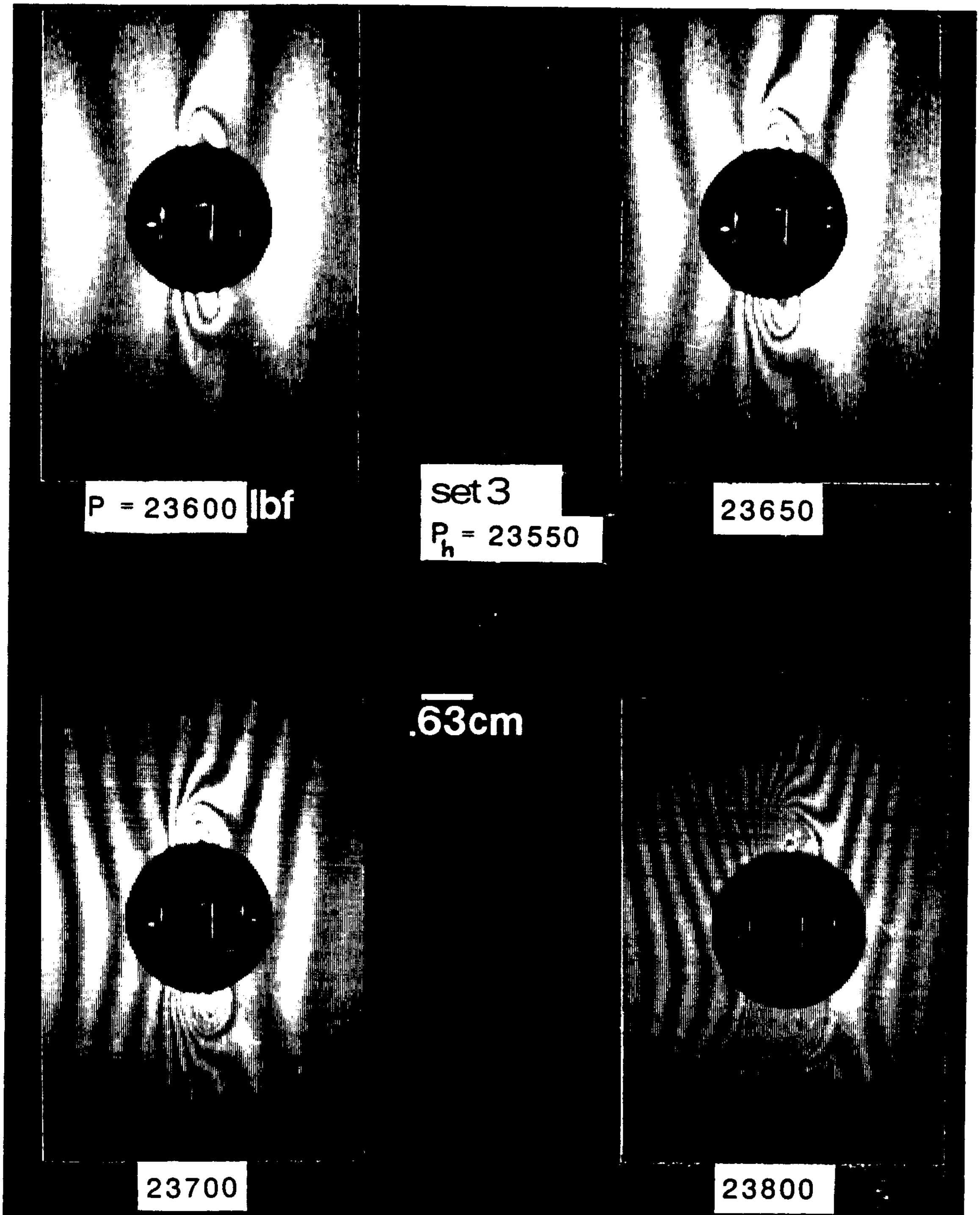

Figure19c. Fringe pattern exhibiting buckling and growth of buckled area

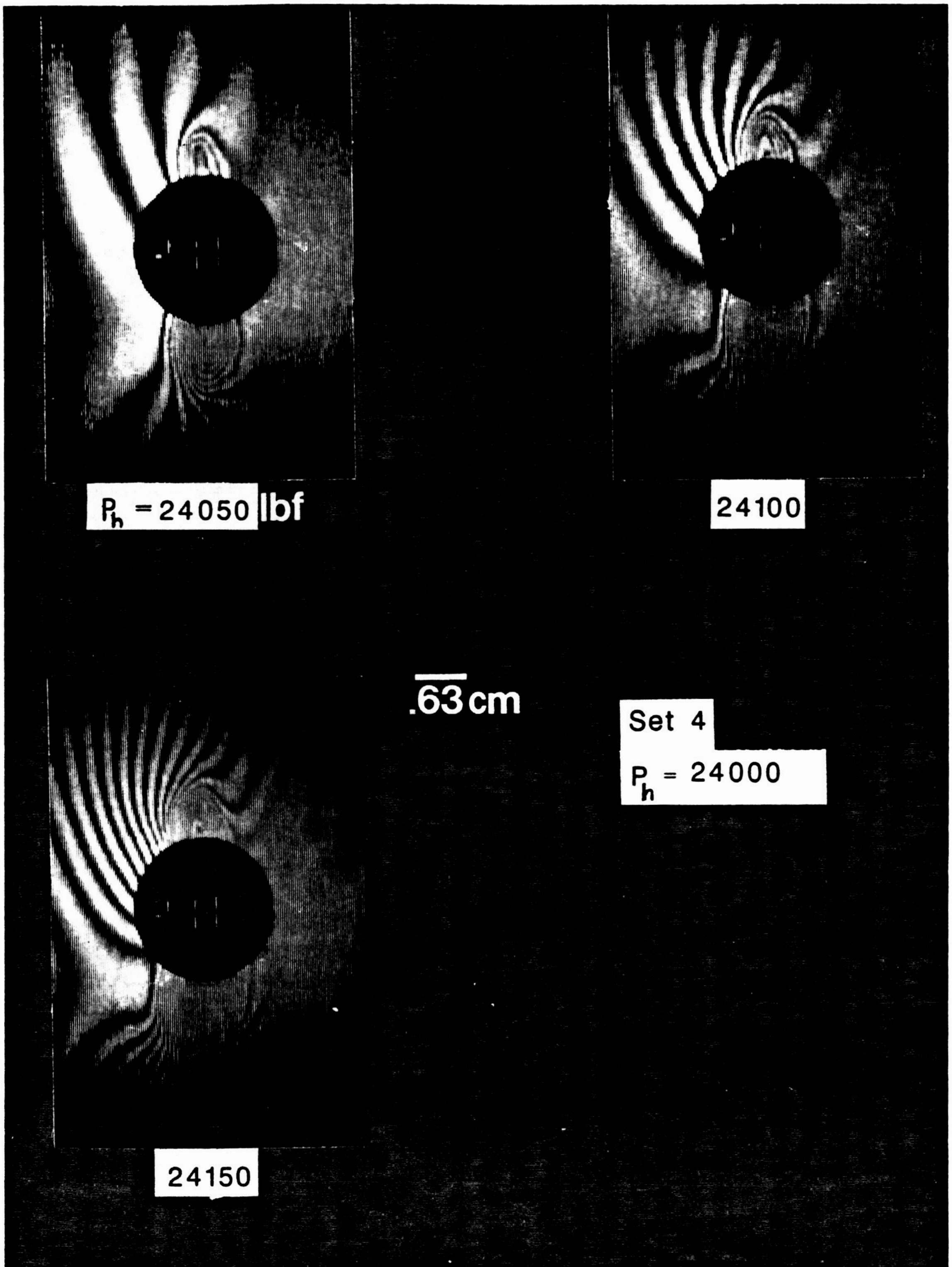

Figure 19d. Fringe pattern exhibiting buckling and growth of buckled area

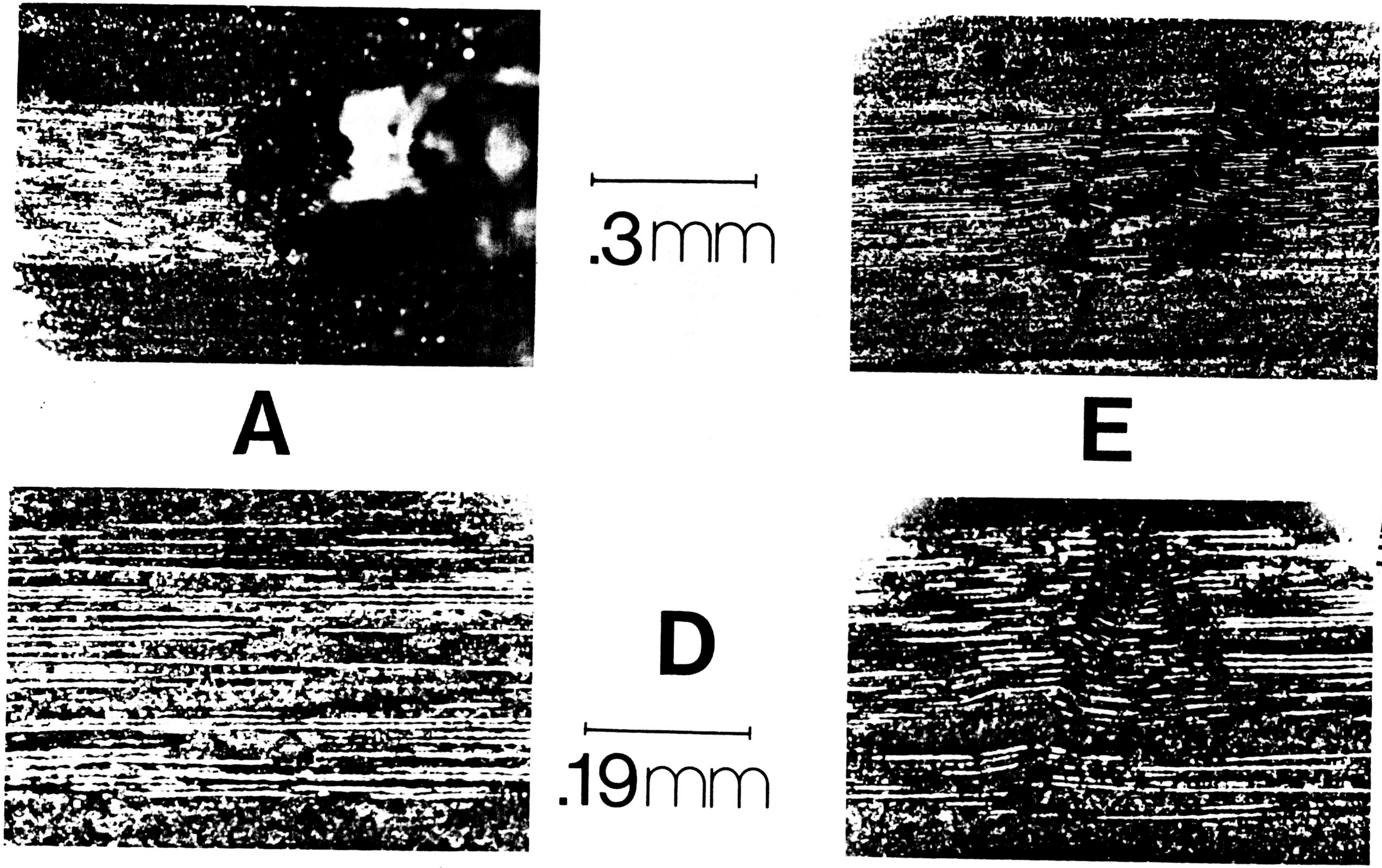

Figure 20. Surface/Internal damage to spec. TB II at different sections

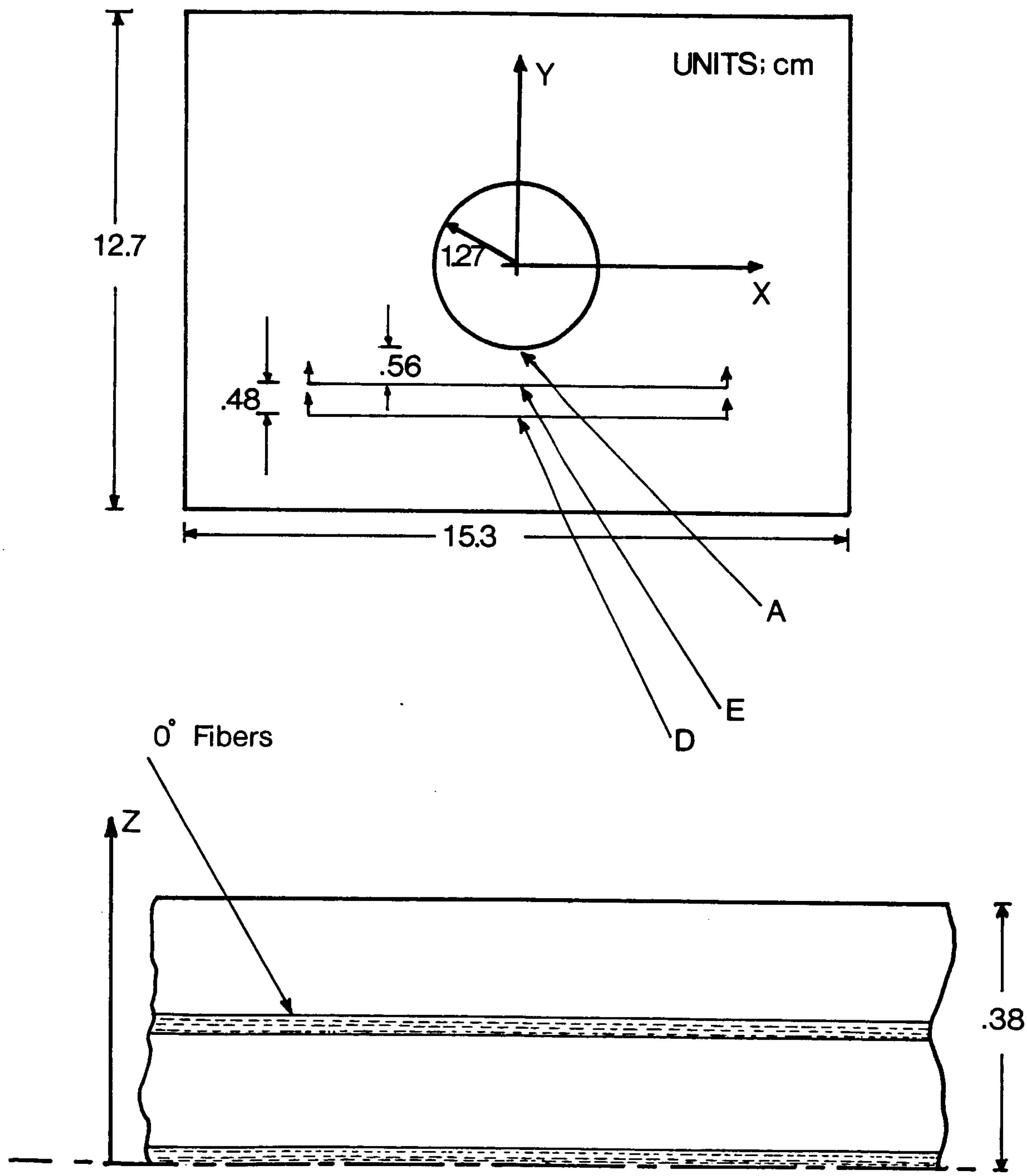

Figure 21. Post-experiment microscopic examination (TB 11)

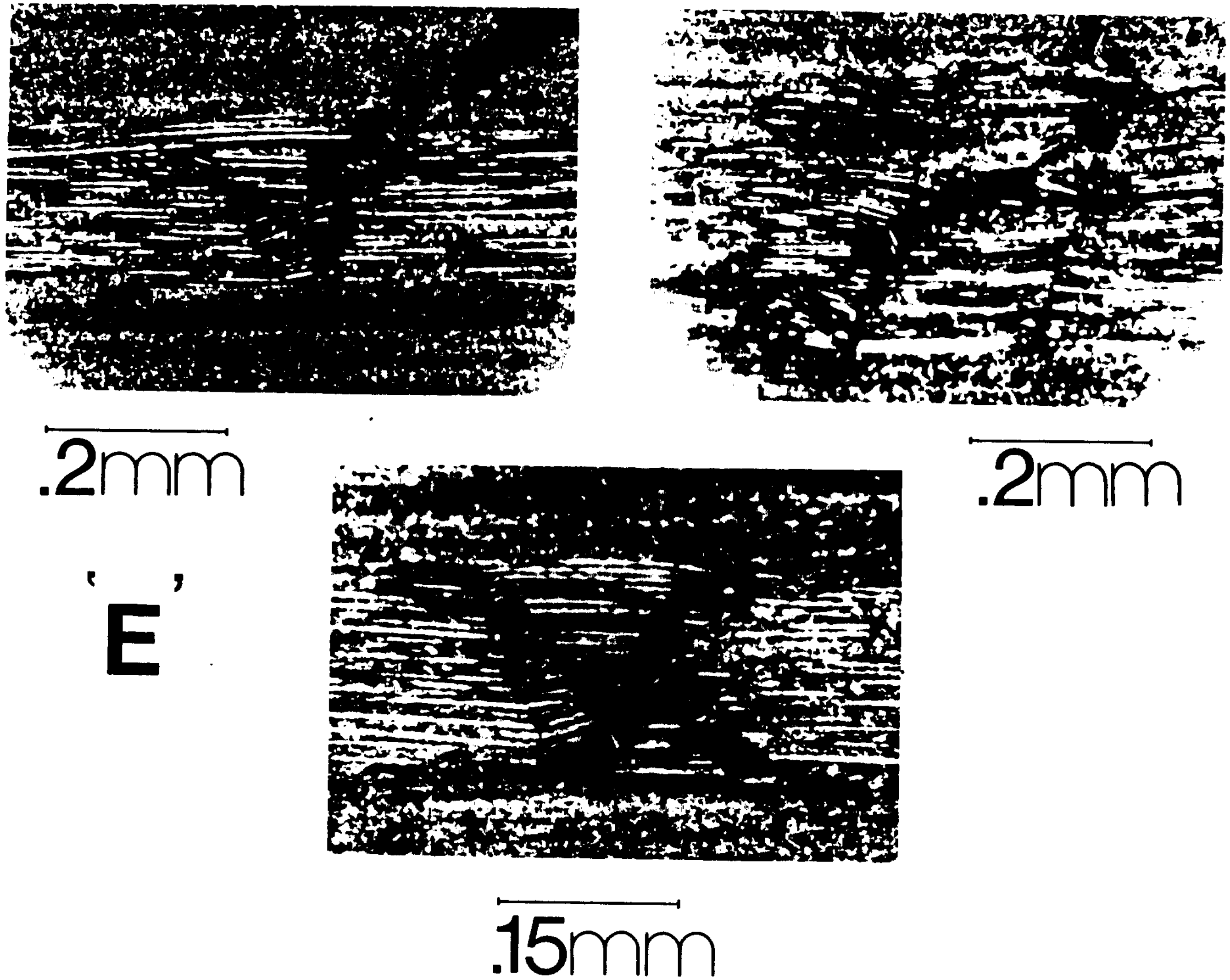

Figure 22. Internal damage at section E (spec. TB II)

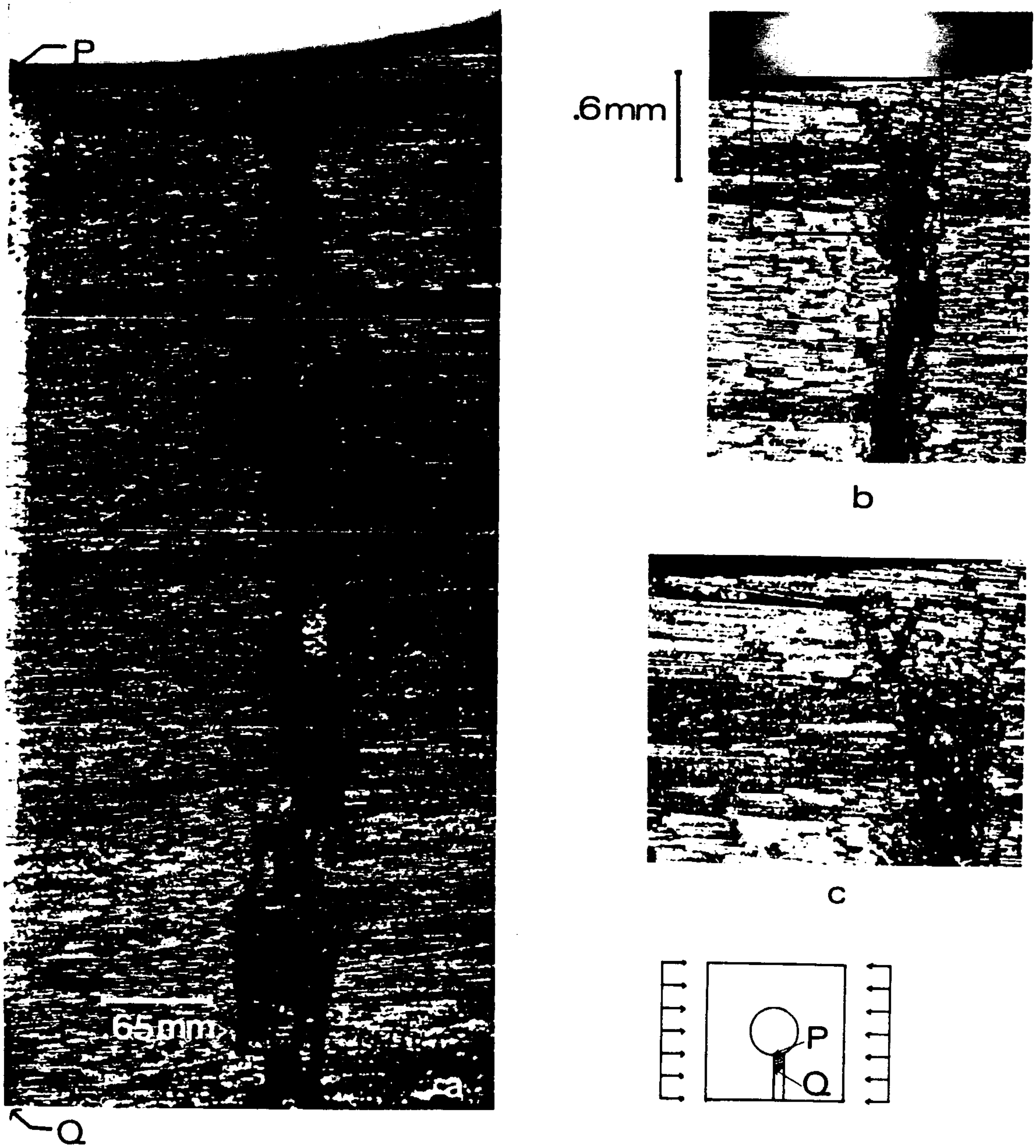

Figure 23. Planform view of internal damage to 0° layers. a) mid plane 0° layer (TB11). b) second from bottom 0° layer (TB17). c) inset of (b).

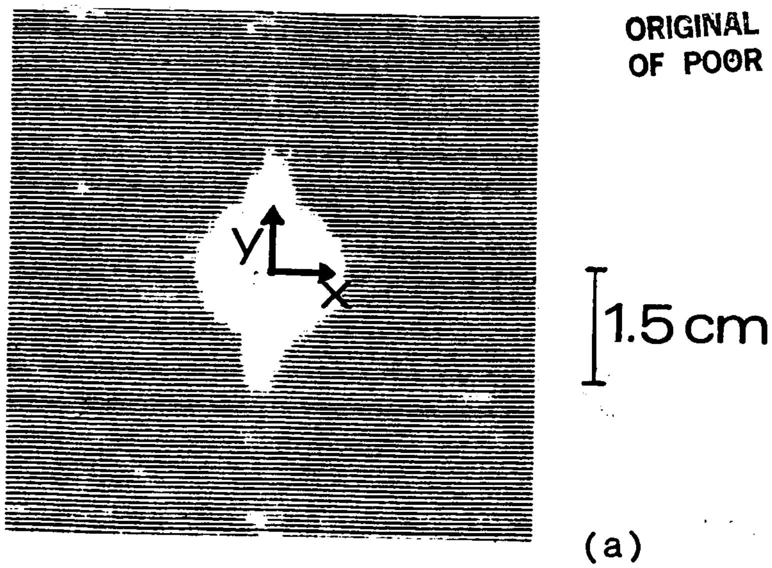

(a)

TB16

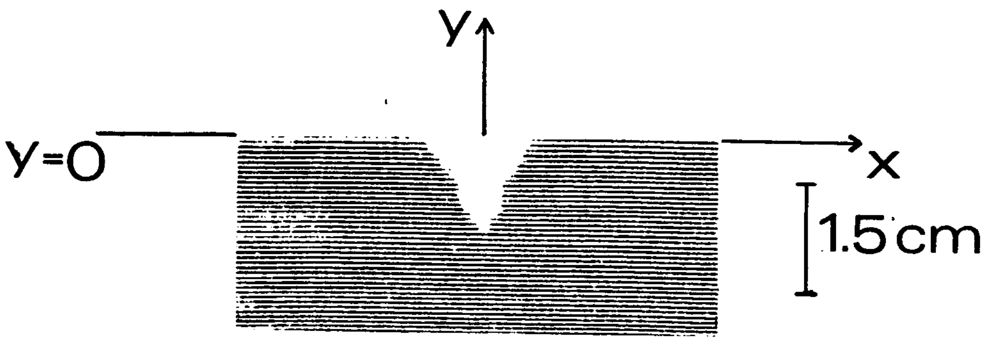

TB15 (b)

load direction— ' x '

Figure 24. C–scan of damaged specimens

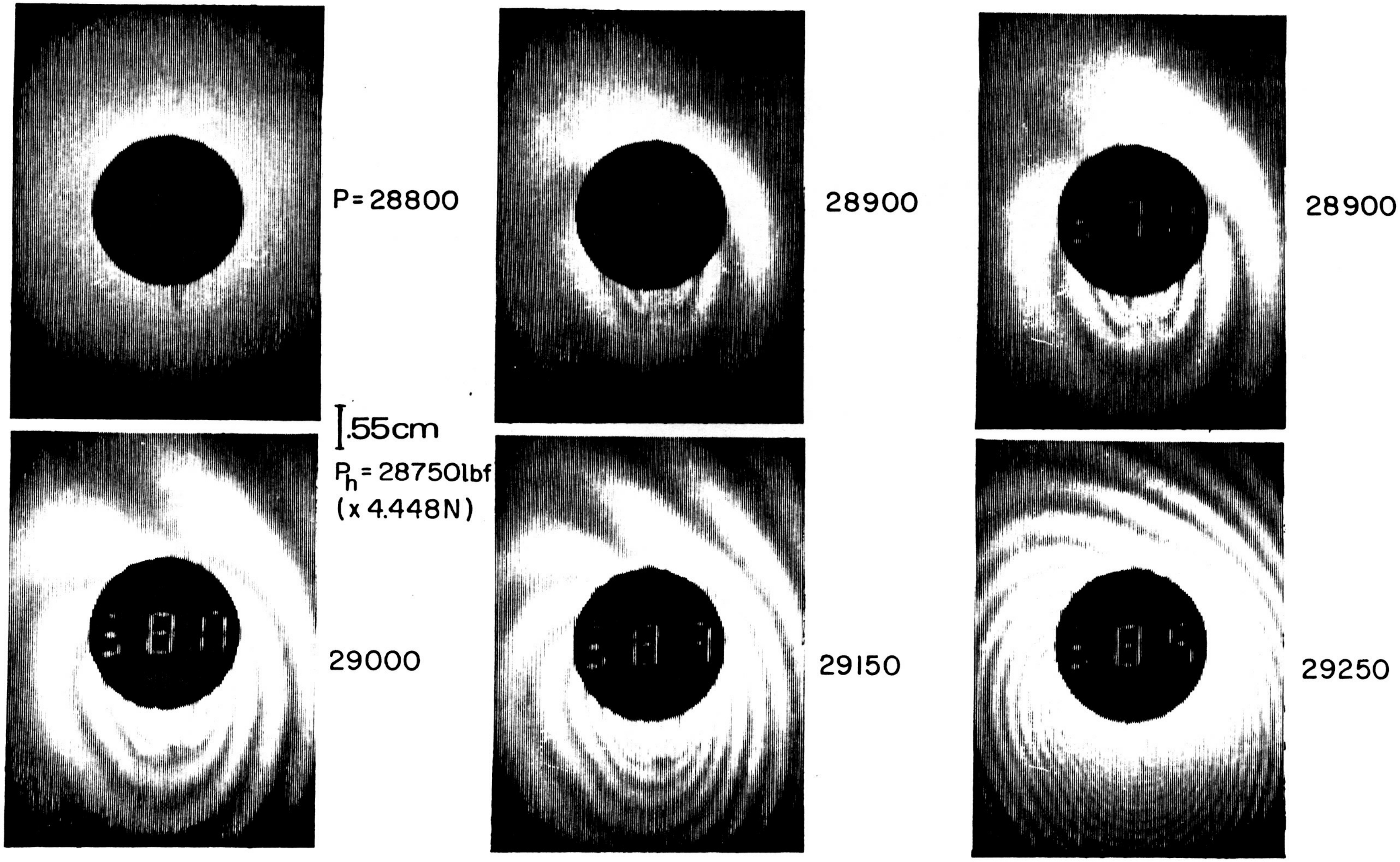

Figure 25. Surface buckle formation on lower half of spec. TB 17

ORIGINAL PAGE IS
OF POOR QUALITY

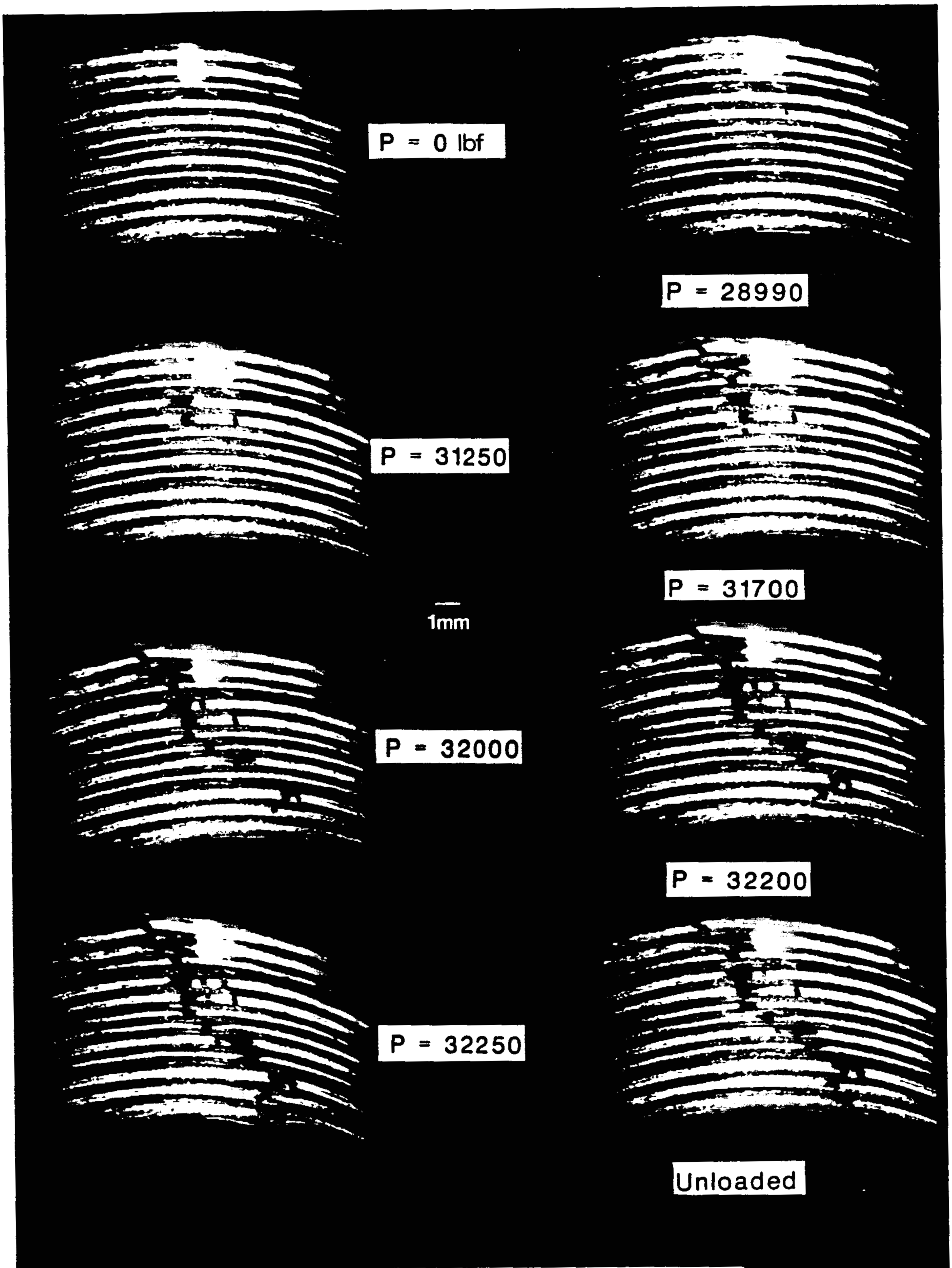

Figure 26. Photomicrographs of hole surface showing damage progression. Spec TB17

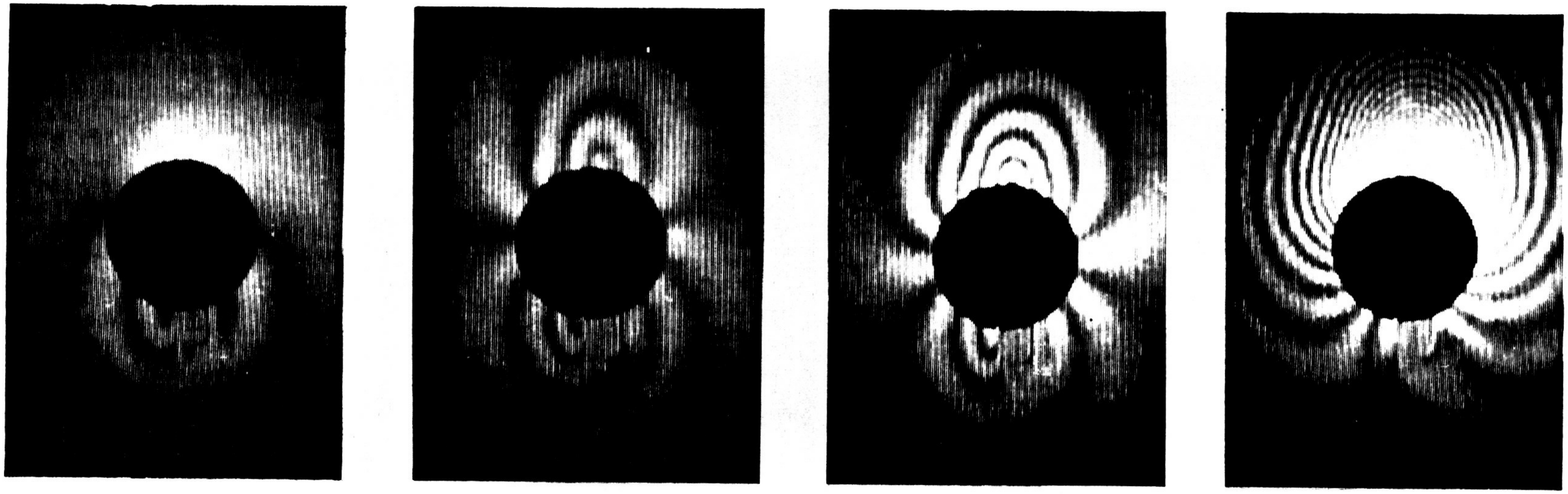

31600 31650 31700 31700

.68cm

P_h = 31550lbf

Figure 27. Initial buckling of surface delamination. (Spec TB17) duration between last two frames is 0.1 sec.

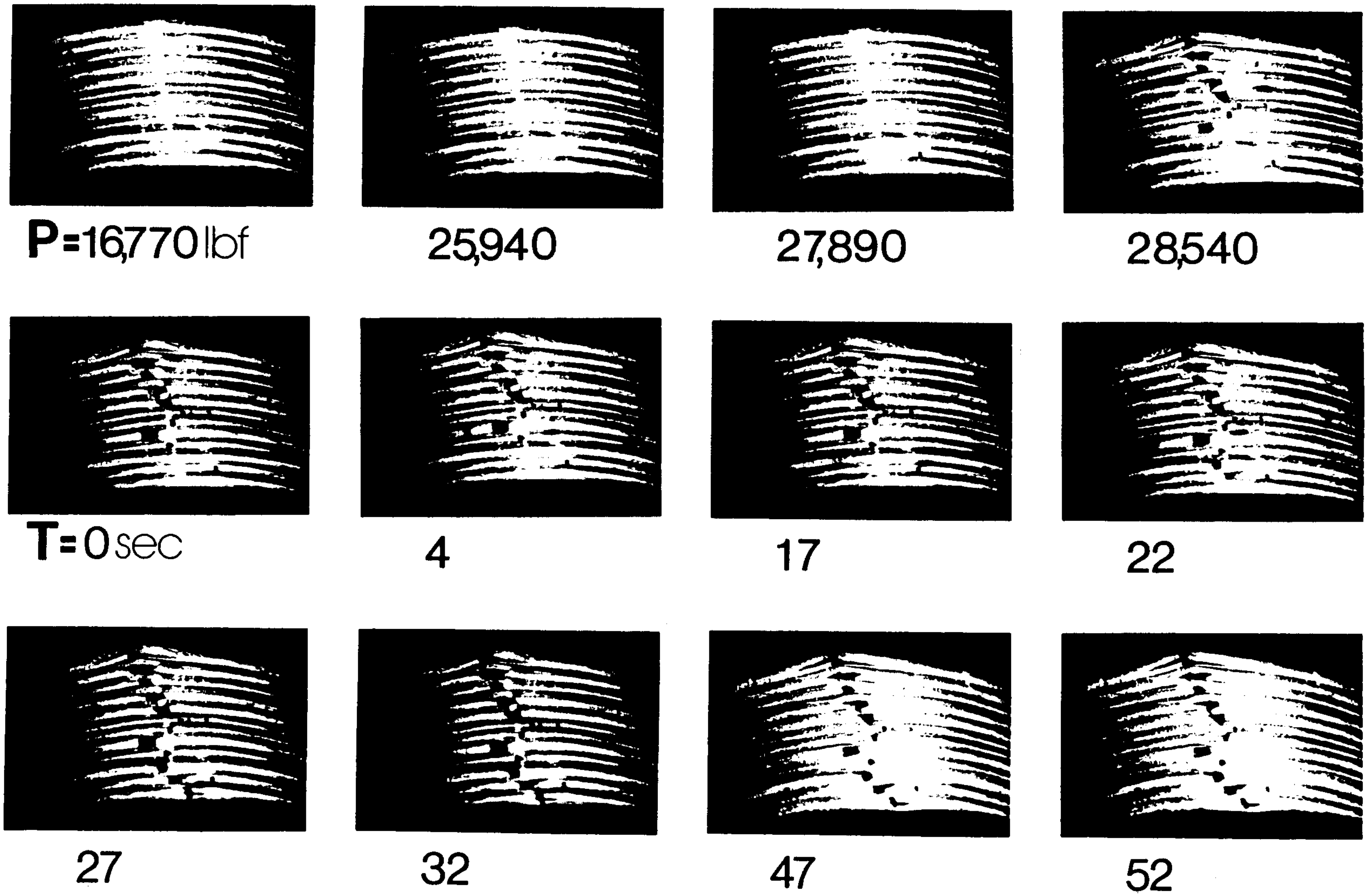

Figure 28. Photomicrographs of hole surface.(TB10)

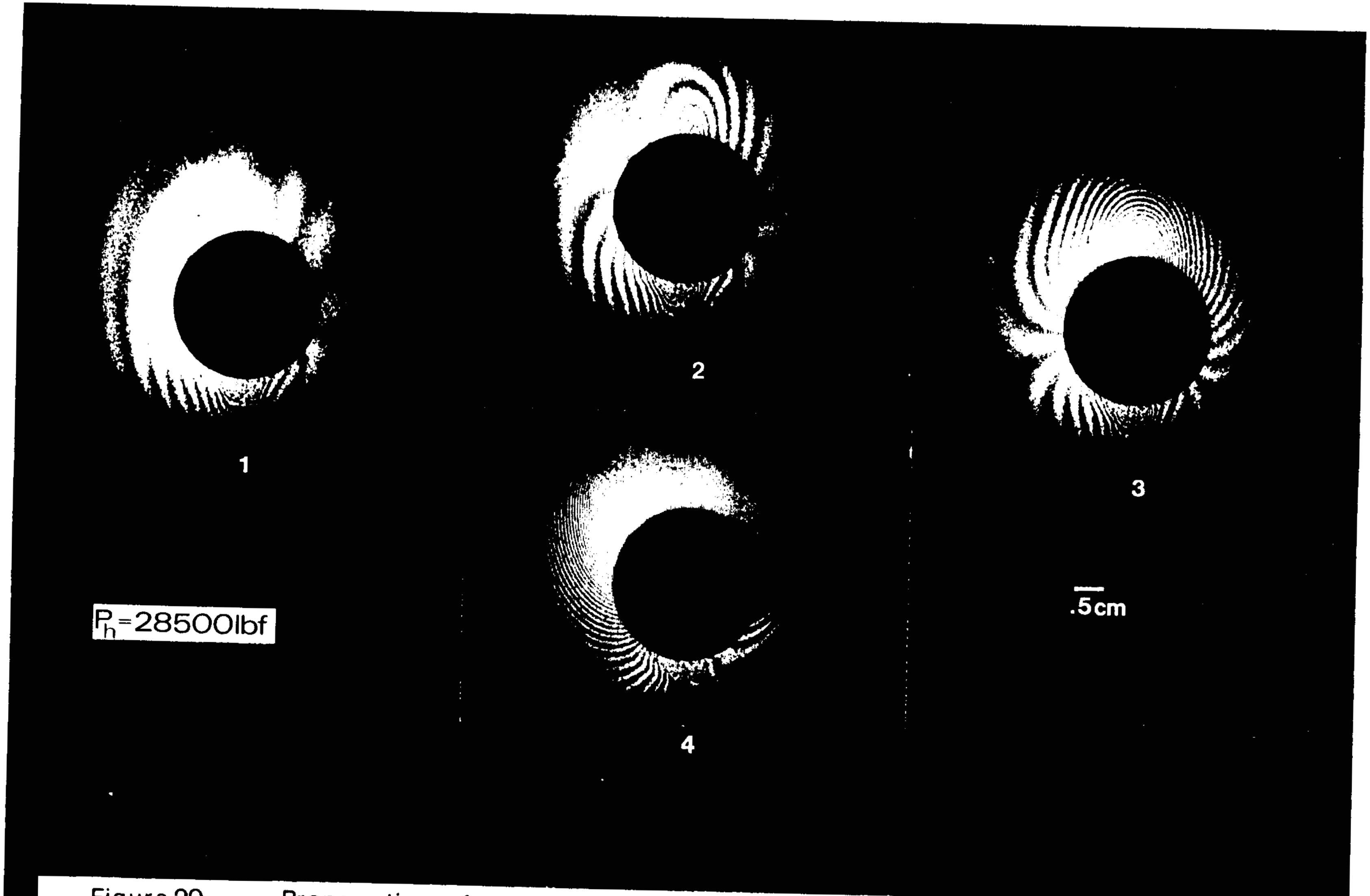

Figure 29. Propagation of surface buckle leading to catastrophic failure. Spec TB1

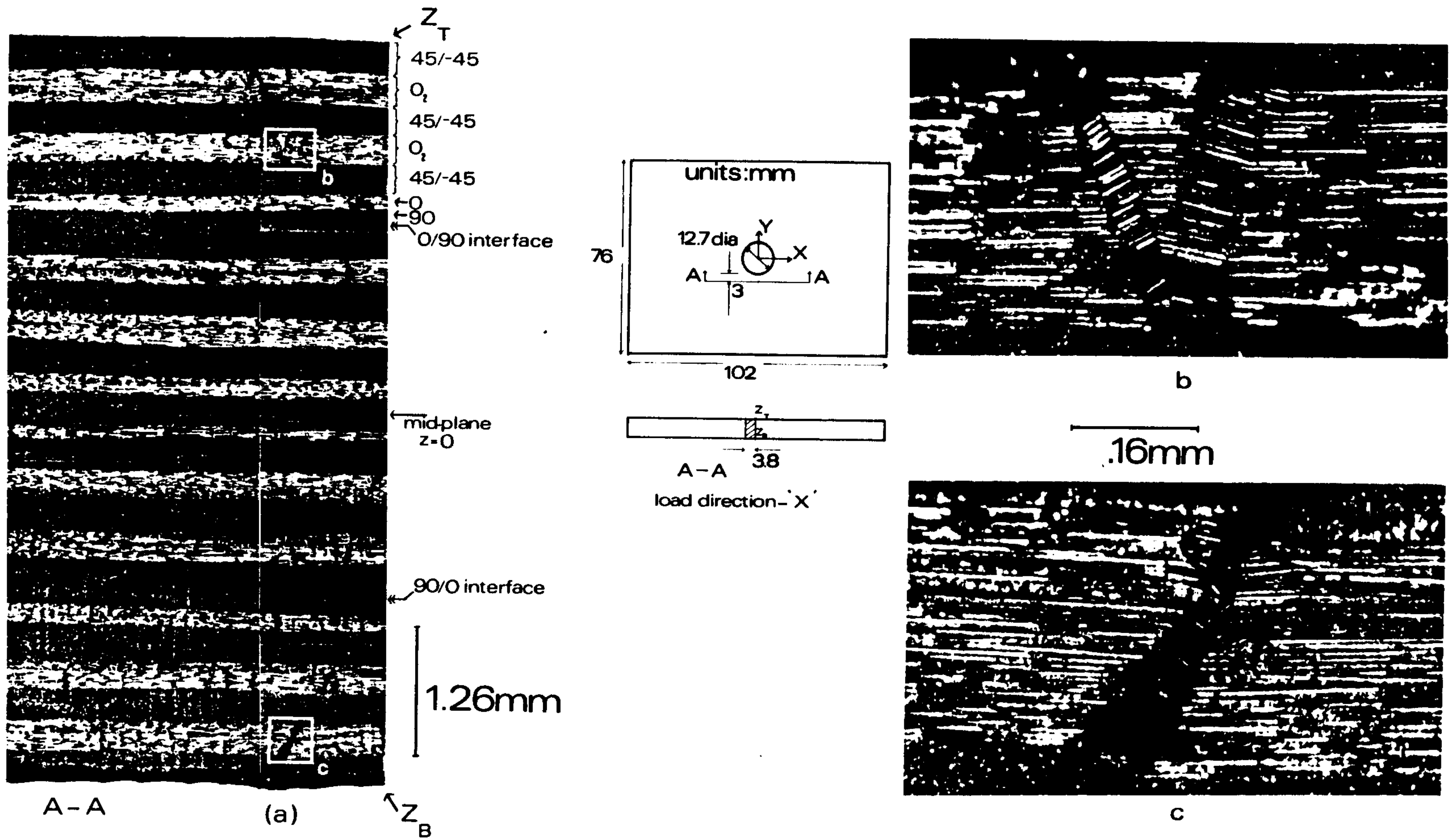

Figure 30. Internal damage at the vicinity of the hole.(spec. TB15) a) Entire cross-section. b) complimentary kink in second 0° layer from top. c) magnified view of damage to bottom 0° layer.

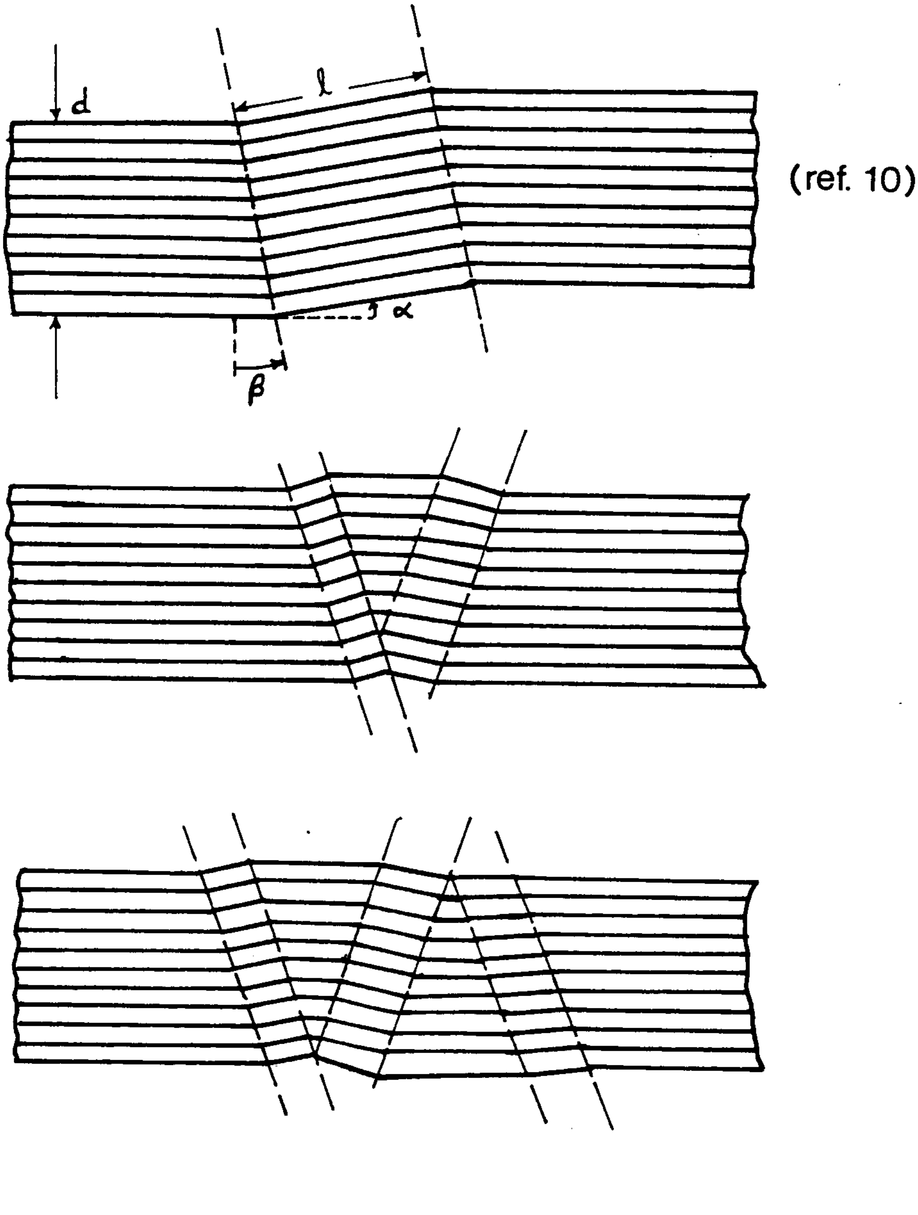

Figure 31. Geometry of a kink band

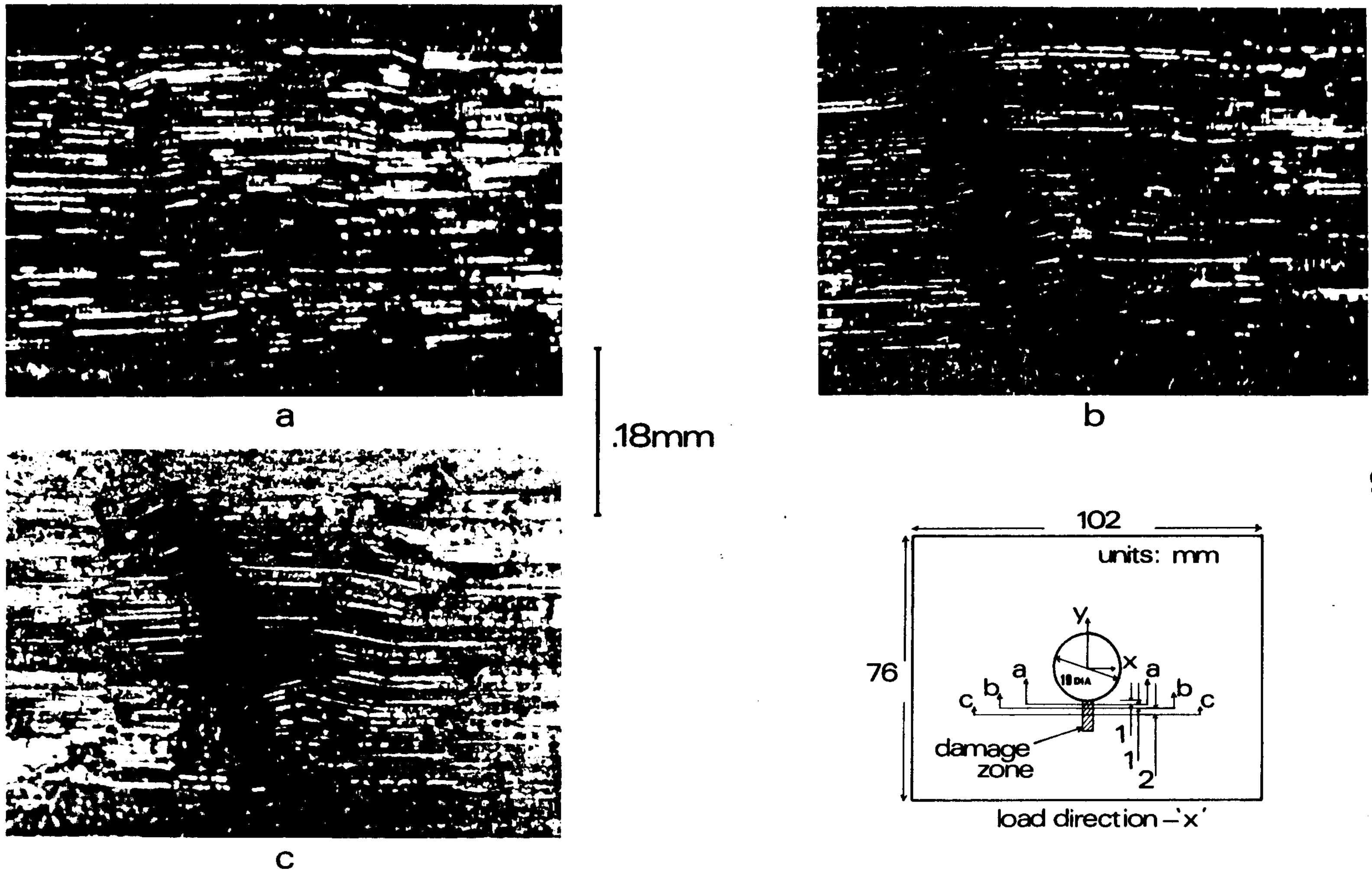

Figure 32. Kink band appearance at different cross sections.(TB17)

a

.36mm

b

.30mm

Figure 33. Sectional study indicating surface delamination (spec. TB 17)

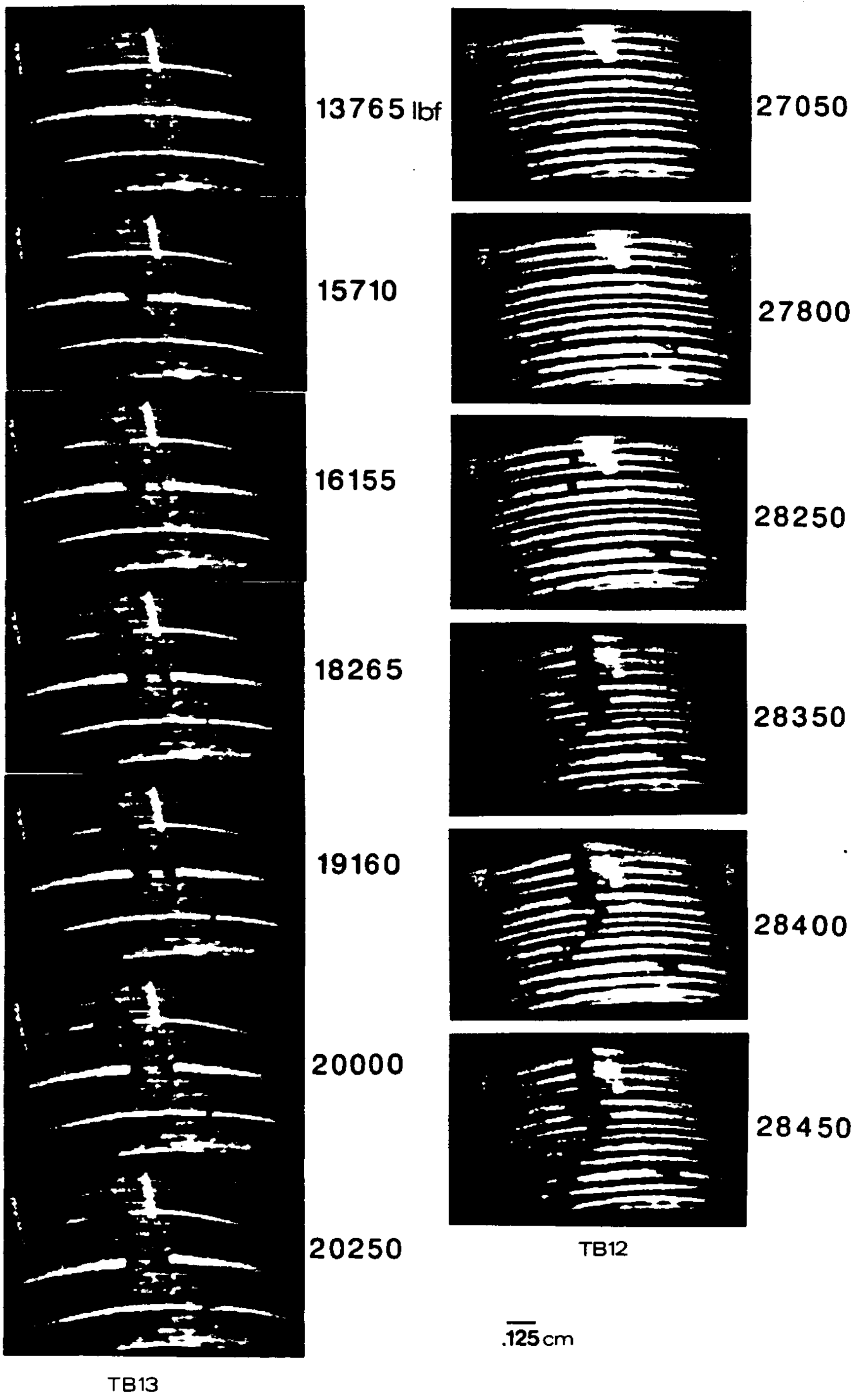

Figure 34. Sequential photomicrographs of hole surface exhibiting damage development.

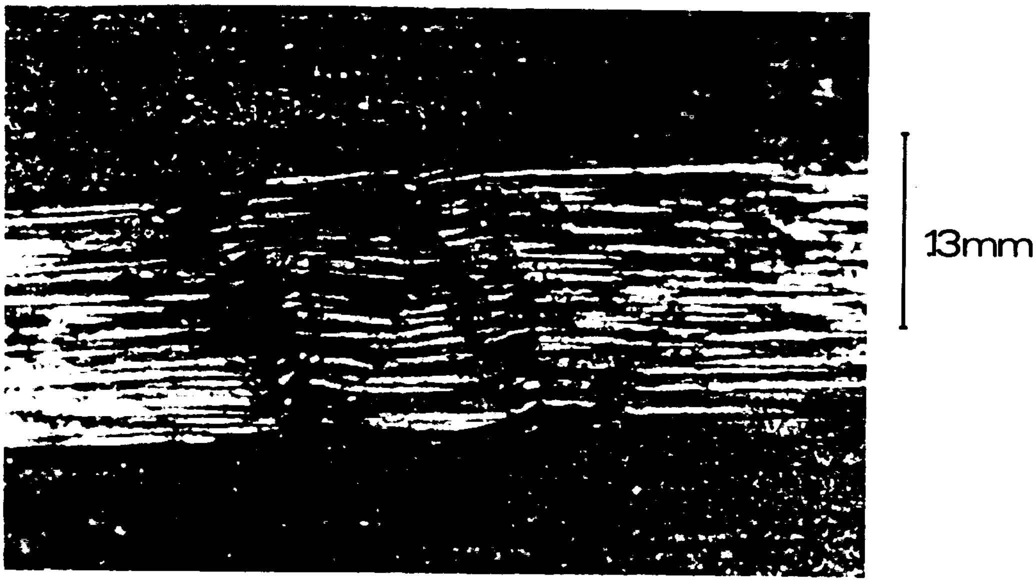

a

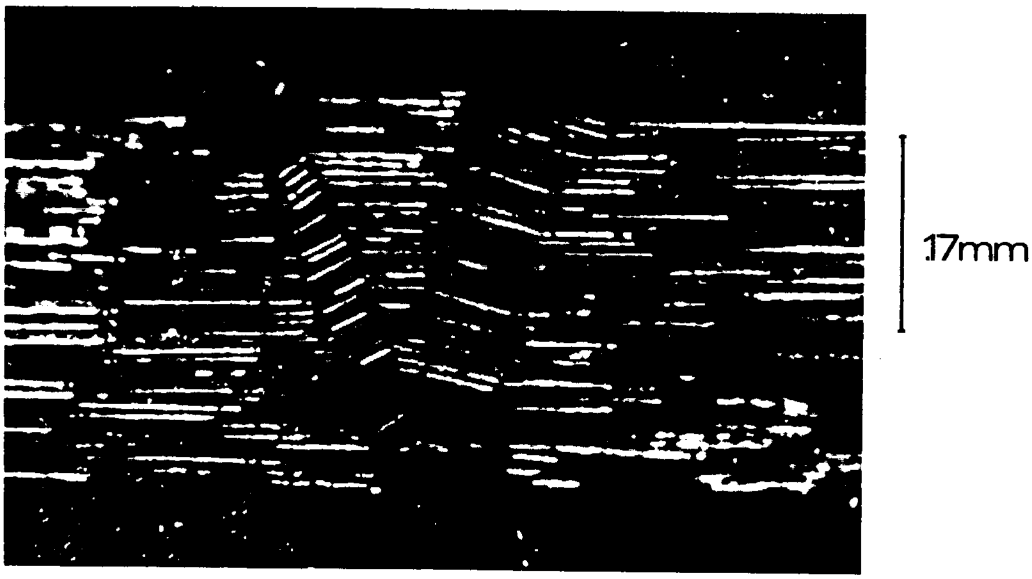

b

Figure 35. Forms of internal damage.

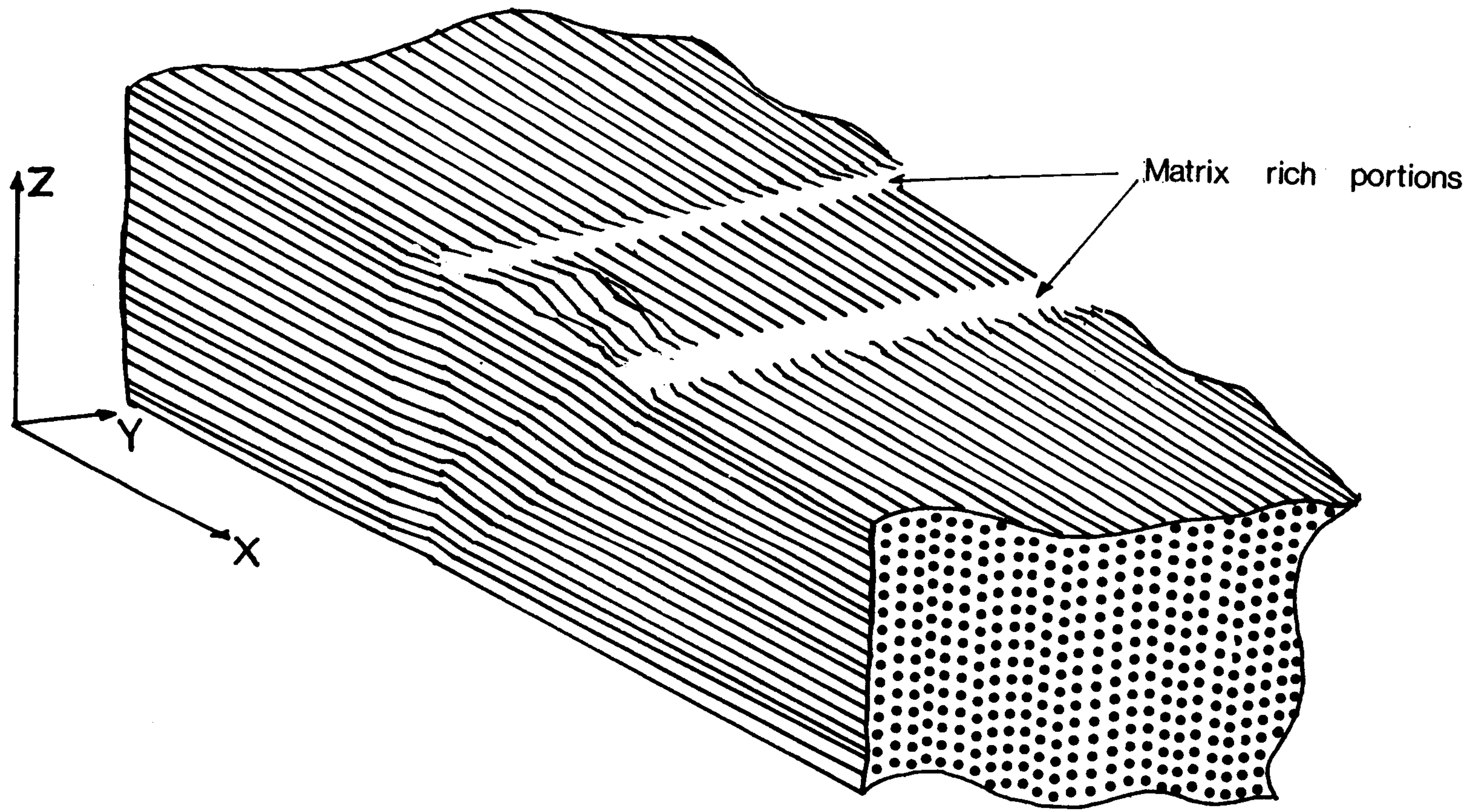

Figure 36. A 3D view of the damage to a zero ply